Additive manufacturing using functional materials

by

SHAHERYAR ATTA KHAN

A Dissertation Submitted to the Graduate School of Sciences and Engineering in
Partial Fulfillment of the Requirements for
the Degree of Doctor of Philosophy

in

Mechanical Engineering

KOÇ ÜNİVERSİTESİ

August 06, 2021

Additive manufacturing using functional materials

Koç University

Graduate School of Sciences and Engineering

This is to certify that I have examined this copy of a doctoral dissertation by

SHAHERYAR ATTA KHAN

and have found that it is complete and satisfactory in all respects, and that any and all revisions required by the final

examining committee have been made.

Committee Members:

PROF. DR. İSMAIL LAZOĞLU (Advisor)

PROF. DR. ERDEM ALACA

PROF. DR. FUNDA ACAR YAĞCI

PROF. DR. M. CEMAL ÇAKIR

PROF. DR. İBRAHIM ETEM SAKLAKOĞLU

Date: August 06, 2021

Dedicated to my family.

ABSTRACT

Additive manufacturing using functional materials

SHAHERYAR ATTA KHAN

Doctor of Philosophy in Mechanical Engineering

August 06, 2021

The ability to additively manufacture using functional materials such as electrically conductive, dielectric, refractory, and hard materials leads to the development of smart and active products. There is a scarcity of functional materials that can be used in the additive manufacturing technique.

In this work, an additively manufacturable and electrically conductive polymer matrix composite (ePMC) is developed and characterized. The electrical conductivity of the developed ePMC is tuneable with a maximum conductivity of 128 $S.m^{-1}$.

An application of the developed ePMC is presented for additive manufacturing a smart disinfection system to contain the spread of SARS-CoV-2.

The thesis also proposes a multi-material additive manufacturing approach for the additive manufacturing of ceramic materials. The proposed approach involves the layer-by-layer additive manufacturing of a negative mold geometry. The ceramic slurry is cast into the mold gradually as it is built up layer-by-layer. The ceramic green body is demolded by dissolving the mold in an organic solvent. The multi-material approach eliminated the shape retention issue of the slurry-based additive manufacturing technique.

ÖZETÇE

Fonksiyonel malzemeleri kullanarak eklemeli üretim

SHAHERYAR ATTA KHAN

Makine Mühendisliği, Doktora

06 Ağustos 2021

Elektriksel olarak iletken, dielektrik, refrakter ve sert malzemeler gibi fonksiyonel malzemeleri kullanarak eklemeli üretim yapabilme yeteneği, akıllı ve aktif ürünlerin geliştirilmesine yol açmıştır. Eklemeli imalat tekniğinde kullanılabilecek fonksiyonel malzeme kıtlığı vardır.

Bu çalışmada, eklemeli üretilebilir ve elektriksel olarak iletken bir polimer matris kompozit (ePMC) geliştirilmiş ve karakterize edilmiştir. Geliştirilen ePMC'nin elektriksel iletkenliği, maksimum 128 S.m-1 iletkenlik ile ayarlanabilir.

Sensör ve aktüatör hibritinin eklemeli üretimi için ePMC uygulaması, SARS-CoV-2'nin yayılmasını önleyen akıllı bir dezenfeksiyon sistemi için sunulmaktadır.

Tez ayrıca, seramik malzemelerin eklemeli imalatı için çok malzemeli bir yaklaşım önermektedir. Önerilen yaklaşım, negatif bir kalıp geometrisinin katman katman eklemeli imalatını içerir. Seramik bulamacı, katman katman oluşturulurken kalıba kademeli olarak dökülür. Seramik yaş gövde, kalıbın organik bir çözücü içinde çözülmesiyle kalıptan çıkarılır. Çok malzemeli yaklaşım, bulamaç(slurry) bazlı eklemeli üretim tekniğinin şekil tutma sorununu ortadan kaldırmıştır.

ACKNOWLEDGEMENTS

I would like to thank Prof. Ismail Lazoglu for the opportunity to work in a world-class research environment at the Manufacturing and Automation Research Center (MARC). The thesis would not have been possible without his constant guidance, support, and motivation.

I thank my research collaborator and dear friend Dr. Anjum Naeem Malik for his support. I am extremely grateful to my fellow MARC members for their friendship and support throughout my doctoral studies. I would especially thank Dr. Caglar Ozturk, Dr. Ismail Enes Yigit, Dr. Omer Subasi, Dr. Mostafa Saleh, Atacan Oral, Dr. Talha Irfan Khan, and Dr. Abasin Ulasyar for their valuable feedback and support.

I am grateful to the staff of the Graduate School of Science and Engineering (GSSE) and the International Community Office (ICO) of the Koc University for their guidance.

I would like to thank my family for forgiving my long absence and taking care of my responsibilities back home. I am grateful to my wife for her patience and support during tough times.

Finally, I am extremely obliged to the Higher Education Commission of Pakistan and Koc University for supporting my doctoral studies.

TABLE OF CONTENTS

LIST OF FIGURES

LIST OF TABLES

Chapter 1

INTRODUCTION

1.1 Additive manufacturing

Additive manufacturing (AM), defined as "the process of joining materials to make parts from 3D model data, usually layer upon layer, as opposed to subtractive manufacturing and formative manufacturing methodologies" [1], is relatively new manufacturing technology. AM was initially developed for prototyping in the 1980s. Since its conception, researchers have developed novel methods, that find applications in aerospace, biomedical, automotive [2], and other fields such as art and fashion. The technology has progressed rapidly from merely a tool for prototyping to a manufacturing process that can produce components of jet engines [3]. AM not only eliminated the need for expensive tooling but also significantly reduces material wastage. The difference between subtractive manufacturing and additive manufacturing is illustrated in Figure 1.1.

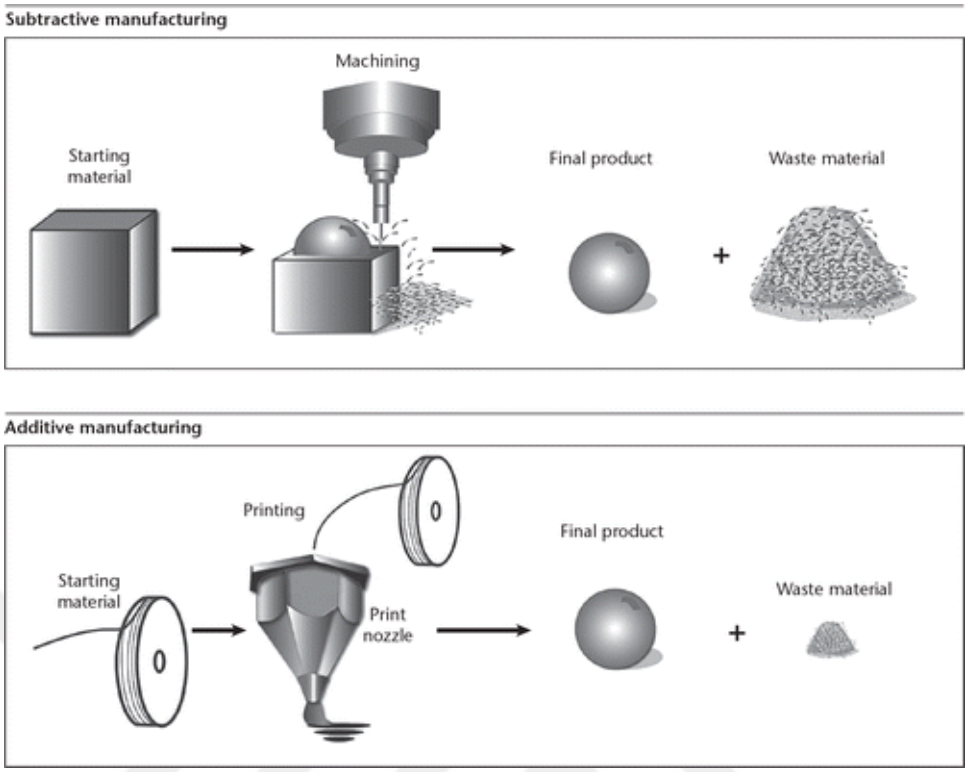

Figure 1.1. Subtractive manufacturing versus additive manufacturing [4].

The additive manufacturing processes are divided into the following groups

1. VAT polymerization
2. Material extrusion
3. Powder bed fusion
4. Directed energy deposition
5. Material jetting
6. Binder jetting
7. Sheet lamination

The types of additive manufacturing are illustrated in Figure 1.2.

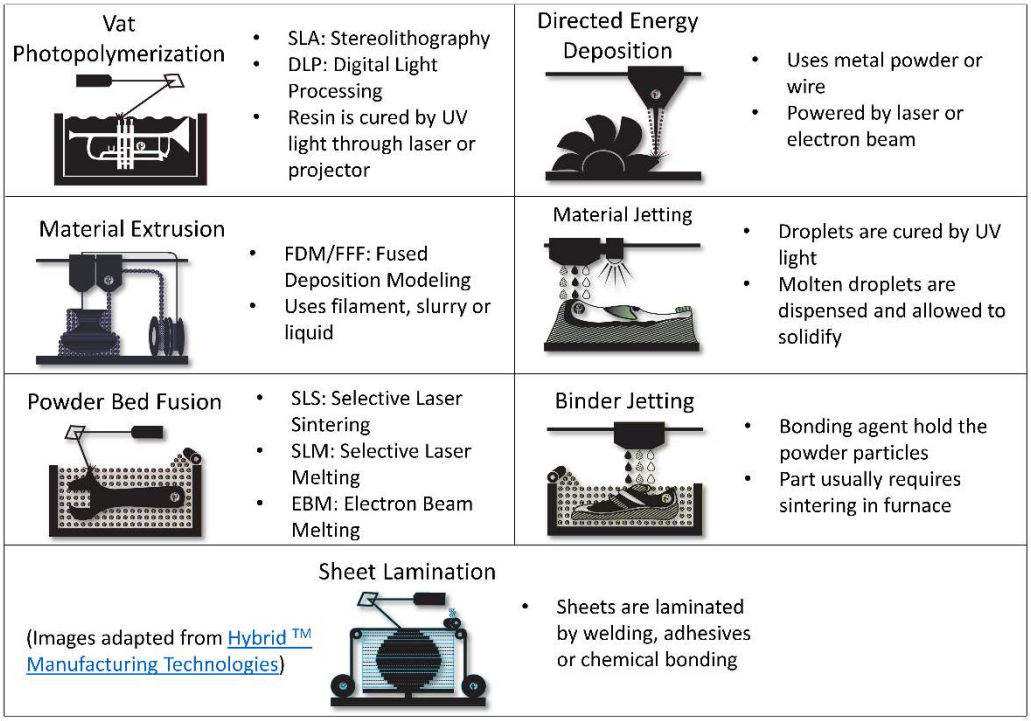

Figure 1.2. The types of additive manufacturing

1.2 Material extrusion

Material extrusion involves the extrusion of the feedstock material through a nozzle mounted on a 3-DOF cartesian manipulator. The schematic of material extrusion is illustrated in Figure 1.3.

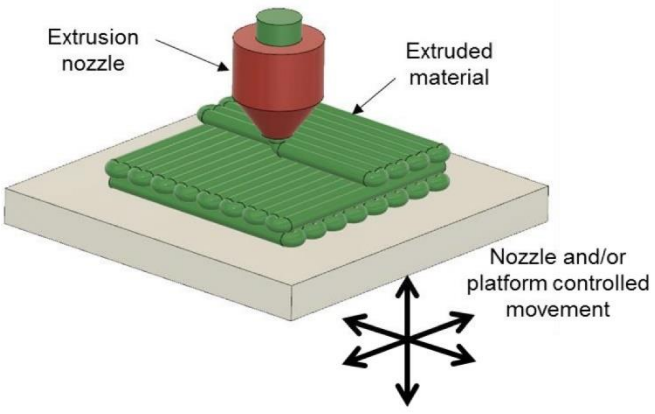

Figure 1.3. Schematic of the material extrusion technique [5].

1.2.1 Filament based material extrusion

The Fused Deposition Modelling (FDM) and Fused Filament Fabrication (FFF), are the most used material extrusion type additive manufacturing technologies. The FDM and FFF utilize a pre-formed thermoplastic filament which is extruded through a heated nozzle. The thermoplastic is extruded at a temperature above its glass transition temperature. The extrudate cools down and solidifies to regain its strength. A typical FFF tool head is illustrated in Figure 1.4.

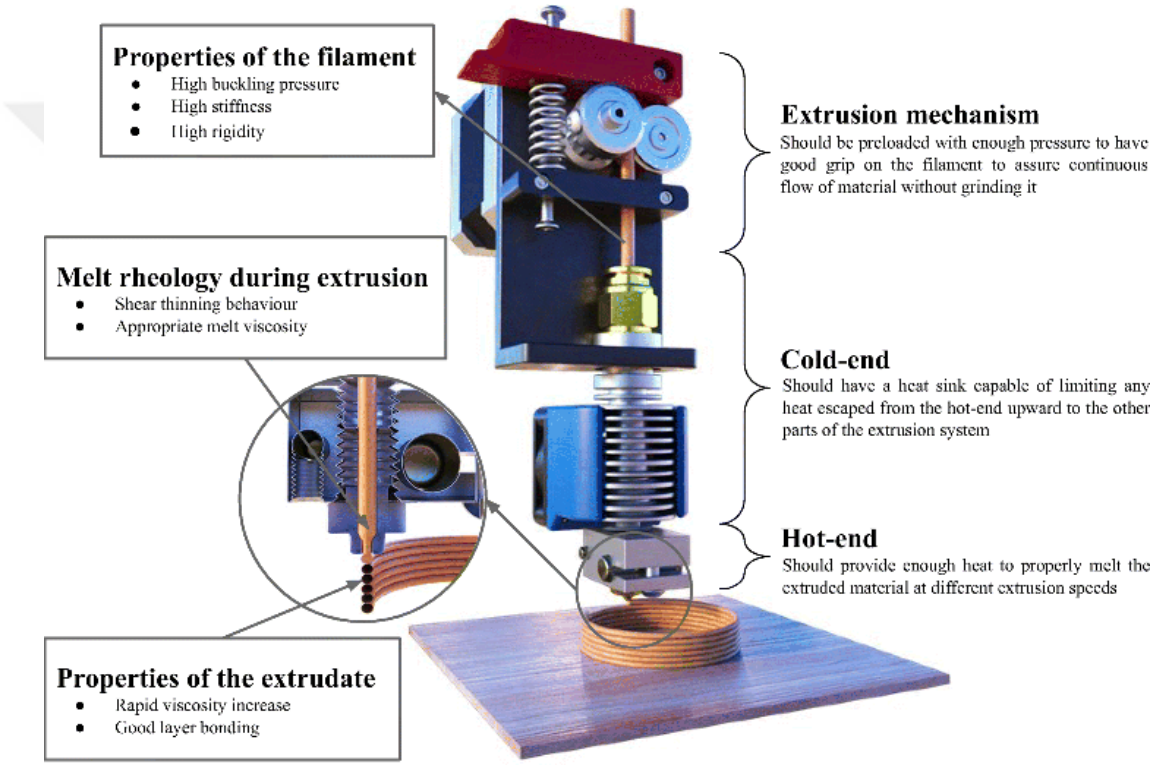

Figure 1.4. Fused filament fabrication (FFF) tool head [6].

The reasons for the popularity of these technologies are their low cost and high manufacturing speeds [7]. The cons of FDM/FFF are a limited range of material, poor surface finish, and the need for a pre-formed filament [8].

1.2.2 Ink based material extrusion

Direct Ink Writing (DIW) is a variant of material extrusion-based additive manufacturing (AM). DIW eliminates the need for a pre-formed filament widely used in extrusion-based AM techniques by depositing viscous pastes called “inks” using a

pneumatic or motorized dispenser and a fine nozzle mounted on a manipulator to selectively deposit inks. The inks have high viscosity and controlled shear thinning properties which makes it easier for the ink to flow through the nozzle. The ink regains its viscosity after it is deposited from the nozzle. The deposited ink is solidified either by the evaporation of solvents or by a curing reaction. Inks with functional properties (such as electrical, mechanical, chemical, and biological) can be deposited using this technique [9]. Figure 1.5 shows a schematic of the DIW process.

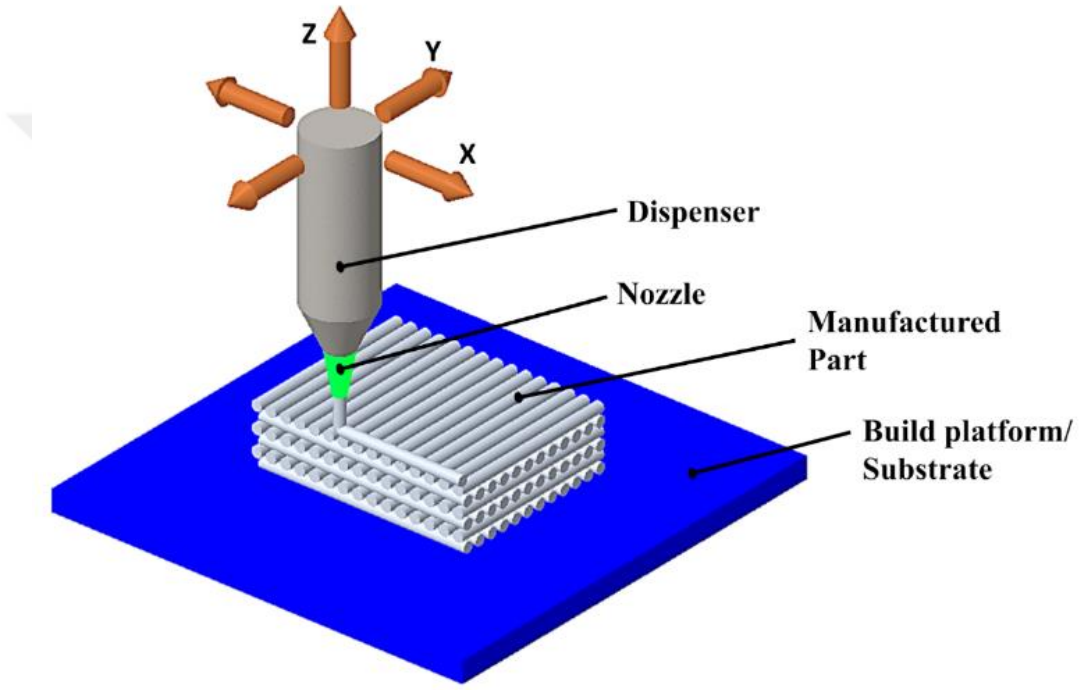

Figure 1.5. Schematic of Direct Ink Writing (DIW) process.

1.3 Robotic additive manufacturing

The conventional material extrusion-based additive manufacturing systems mostly employ a stepper motor-based belt pulley mechanism for the X and Y axes, and a lead screw mechanism for the Z-axis. These stepper motors operate in an open-loop without any positional feedback and therefore, positional inaccuracies in the built part are a common occurrence due to missed steps.

Robotic manipulators employ servo motors which operate in a closed-loop providing feedback on the position and speed of the motor. The robotic manipulators are highly precise with their typical precision ranging from 100 µm to 10 µm. In addition to their

precision, robotic manipulators are available in the market for various payload capacities and working spaces. Therefore, robotic manipulators are being widely adopted for additive manufacturing large-scale additive manufacturing as well as precision additive manufacturing.

1.4 Multi-material additive manufacturing

Multi-material additive manufacturing refers to the ability to selectively deposit dissimilar materials in one additive manufacturing build. For instance, an additively manufacturing setup that can deposit electrically insulating and conductive regions in one single build is referred to as a multi-material additive manufacturing setup.

1.5 The MARC multi-material robotic additive manufacturing setup

The MARC multi-material robotic additive manufacturing setup comprises a FFF deposition head and a DIW deposition head mounted on a Mitsubishi robotic manipulator. The FFF head enables the setup to deposit thermoplastic materials such as polylactic acid (PLA), acrylonitrile butadiene styrene (ABS), and glycol-modified polyethylene terephthalate (PETG). The DIW head enables the deposition of functional materials such as electrically conductive polymer composites and ceramic slurries. The resolution of the robotic manipulator is 10 µm with a payload capacity of 2 kg and a reach of 700 mm. The MARC multi-material robotic additive manufacturing setup is illustrated in Figure 1.6.

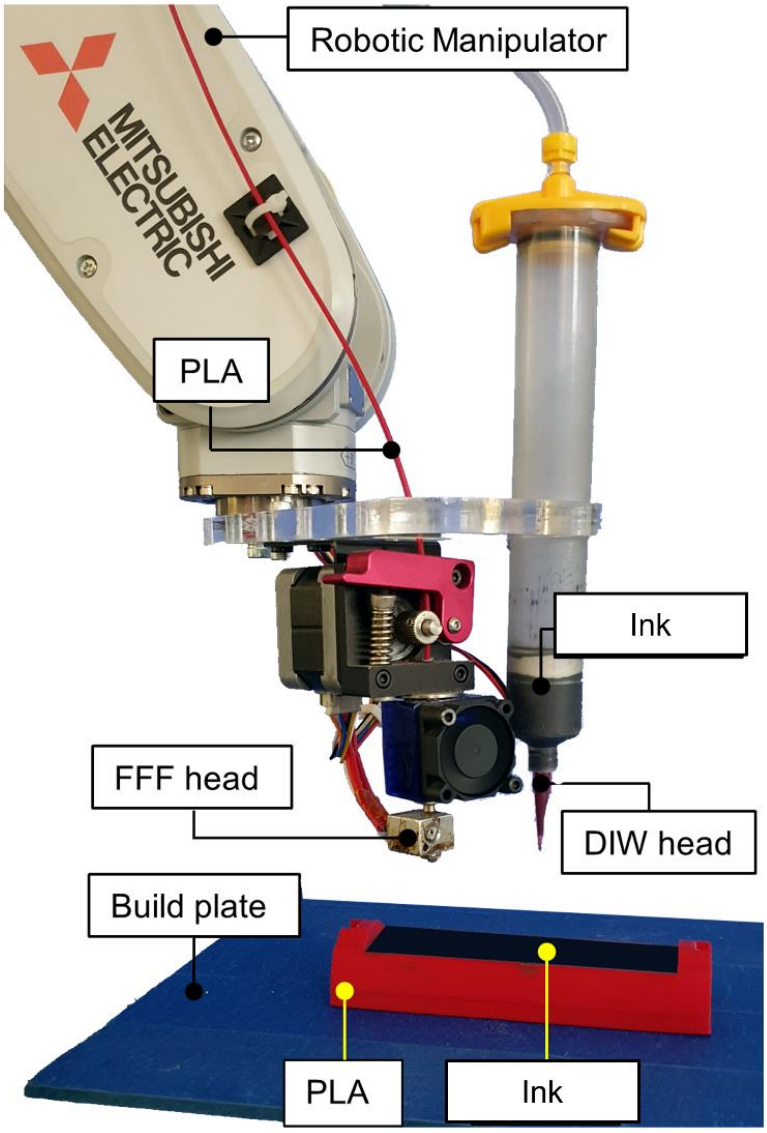

Figure 1.6. The MARC multi-material robotic additive manufacturing setup.

1.6 Process flow robotic additive manufacturing

The process flow of robotic additive manufacturing starts from CAD geometry. The CAD geometry is processed through a slicing engine to generator the Gcode which is the generic toolpath file accept by most commercially available additive manufacturing systems. In course of this research, an open-source slicing engine commonly known as Ultimaker Cura was adopted. The robotic manipulators cannot be controlled using the G-codes and therefore, the G-codes must be post-processed to conform to the programming language of the robotic manipulator. The Mitsubishi robotic manipulator is programmed using a proprietary Melfa language and therefore, a MATLAB script was coded to post-

process the generated Gcode into Melfa compliant robot toolpaths. The toolpaths are then sent to the controller of the robot to manufacture the final part. The process flow of robotic additive manufacturing is illustrated in Figure 1.7.

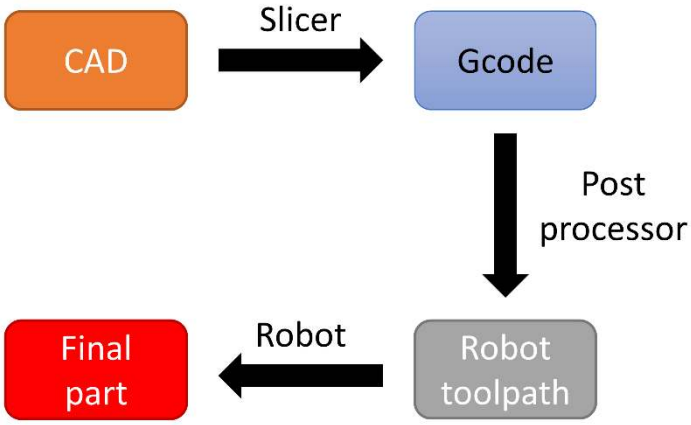

Figure 1.7. The process flow of robotic additive manufacturing.

1.7 Significance of additive manufacturing with functional materials

Materials that have one or more properties that respond to an external stimulus such as mechanical, electrical, and chemical stimuli are called functional materials. Examples of functional materials are semiconductors, ionic conductors, viscoelastic fluids, dielectric materials. Functional materials are widely used in engineering applications especially in the development of sensors and actuators.

The ability to additively manufacture using functional material has the potential to open a new domain of smart and functional additive manufacturing. For instance, electrically conducted functional material that is additively manufacturable may lead to the development of sensors, such as capacitive sensors. Moreover, additive manufacturing allows the realization of complex geometries that can not be manufactured using conventional techniques. Therefore, functional parts in application geometries can be manufactures by the integration of additive manufacturing and functional materials.

1.8 Research aim

This thesis aims to develop additively manufacturable functional material and layout the process flow for additive manufacturing with functional materials. The following are the objectives of this thesis.

- To develop a novel electrically conductive material for additive manufacturing.
- To demonstrate the ability to develop additively manufacturable sensors and actuators.
- To develop a process for the additive manufacturing of engineering ceramics.
- Finally, to highlight the issues faced during this research and present suggestions for future work.

1.9 Thesis outline

The thesis discuss the additive manufacturing of an electrically conductive material and the multi-material additive manufacturing technique for the manufacturing of dense ceramic bodies.

The thesis is divided into seven chapters. Chapter 2 lays out the background and literature review of additive manufacturing with electrically conductive materials and ceramics. Chapter 3 discusses the development of graphite-based electrically conducive polymer composite, its characterization, and its applications for the development of sensors and actuators. Chapter 4 discusses the additive manufacturing of a smart disinfection system. Chapter 5 discusses the additive manufacturing of ceramics using a multi-material approach. Finally, chapter 6 provides the conclusion and presents opportunities for future work

Chapter 2

BACKGROUND

2.1 Introduction

The literature review of additive manufacturing with functional materials is divided into two sections. The first section deals with the review of the literature on additive manufacturing with electrically conductive materials and the second section deals with the additive manufacturing of ceramic materials.

2.2 Electrically conductive material for additive manufacturing

The selective deposition of electrically conducting and insulating material within one additively manufactured part has the potential to open a new domain of customized, smart, and active products. Electrically conductive structures, resistors, and capacitors can be produced inside an additively manufactured part by coupling an electrically conductive PMCs (ePMCs) AM head with an insulating AM head [10]. Products such as antennas can be additively manufactured with the ability of electrically conductive AM [11, 12].

Various contributions have been made towards the development of ePMCs for AM. Wei et al. prepared an ePMC filament by melt mixing ABS and graphene and demonstrated its AM using the FFF technique. The study reported a max electrical conductivity in the order of 10^{-2} $S.m^{-1}$ [13].

Tan and Low prepared various ePMC filament for FFF by loading nylon and polyethylene with nickel and solder alloy. The highest electrical conductivity of the

ePMC filaments was reported to be 104 $S.m^{-1}$, however, only 10% of the electrical conductivity was retained in the additively manufactured part [14].

Singh et al. loaded an ABS matrix with graphite and demonstrated the AM ePMC filaments. The study, however, did not characterize the electrical conductivity [15].

Sezer and Eren prepared ePMC filaments by loading ABS with multi-walled carbon nanotubes. The study reported an electrical conductivity of 232 $S.m^{-1}$ for the ePMC filament, however, only 10 $S.m^{-1}$ was retained in the final manufactured part [16].

Previous studies [13–16] have opted for the preparation of an ePMC filament due to the popularity of the FFF technique; however, the preparation of an ePMC filament requires the melt mixing of the matrix polymer and the reinforcement. This melt mixing is performed at temperatures beyond the glass transition temperature of the matrix polymer and requires specialized equipment such as single/twin-screw extruders. Nevertheless, the rheology of the ePMC must be tailored to achieve extrudability from the FFF nozzle. Furthermore, the electrical conductivity of an additively manufactured part is significantly less compared to that of the ePMC filament used in the process as observed in the previous studies [14, 16]. This reduction in the electrical conductivity indicates that the homogeneity of the ePMC achieved by the melt mixing is disturbed on extrusion from the FFF nozzle.

The preparation of an ePMC filament can be eliminated by using DIW. ePMCs in the form of inks can be used in AM to produce electrically conductive structures for applications such as electrochemical sensing [17] and strain sensors.

Farahani et al. demonstrated the DIW of carbon nanotube-loaded epoxy with an electrical conductivity of 10^{-4} $S.m^{-1}$ [18]. Zhong et al. performed DIW of graphene oxide-loaded geopolymers and reported an electrical conductivity of 10^{2} $S.m^{-1}$ [19]. Areir et al. loaded polyvinyl alcohol hydrogels with activated carbon for DIW, however, the electrical conductivity of the hydrogel was not characterized [20].

The studies [18–20] demonstrated the potential of ePMCs in DIW. The homogeneity achieved in the preparation of the ePMC is not disturbed during the process as there is no remelting involved.

Table 2.1 provides a summary of AM using ePMCs from previous studies.

Table 2.1. Examples of ePMCs utilized in additive manufacturing from literature

Contributors	AM Technique	Material	Max. electrical conductivity
Wei et al. [13]	FFF	ABS - graphene	10^{-7} – 10^{-2} S.m^{-1}
Tan and Low [14]	FFF	Nickel – nylon Nickel – polyethylene Solder alloy – nylon Solder alloy – polyethylene	104 S.m^{-1} (However, at most 11% of it was retained after AM)
Singh et al. [15]	FFF	ABS – graphite	Not characterized
Sezer and Eren [16]	FFF	ABS – multi-walled carbon nanotube (MWCNT)	232 S.m^{-1} (reduced to 10 S.m^{-1} after AM)
Farahani et al. [18]	DIW	Epoxy – carbon nanotube (CNT)	10^{-4} S.m^{-1}
Zhong et al. [19]	DIW	Geopolymer – graphene oxide	10^{2} S.m^{-1}
Areir et al. [20].	DIW	Polyvinyl alcohol (PVA) – activated carbon	Not characterized

Various carbon, graphene, and copper-based ePMC filaments have made their way to the market [21–23]. Furthermore, the copper particles are susceptible to oxidation during the FFF process due to the processing temperature of ePMC filaments (130 ˚C – 160 ˚C). Nevertheless, copper tends to oxidize at room temperature, which can lead to a further reduction in the electrical conductivity of the additively manufactured part during its service.

ePMCs with metallic reinforcements have higher electrical conductivities as compared to carbon-based reinforcements. However, the high cost of micro-sized metallic powders, high density, and the tendency to oxidize diverts the attention to non-metallic carbon-based reinforcements. CNTs and graphene reinforcements require special synthesis and off-the-shelf CNT and graphene particles are expensive. Graphite, on the other hand, is readily available in micro-sized particle form at a low cost which makes it an attractive reinforcement material for the development of ePMCs.

Cellulose and its derivatives have been used to develop ePMCs [24]. Sodium carboxymethylcellulose (CMC), a derivative of cellulose, is a water-soluble polymer widely used as a binder in various electrochemical applications including Li-ion batteries [25]. The aqueous solution of CMC demonstrates non-Newtonian shear thinning behavior [26], which encourages the investigation of the suitability of CMC-based ePMC inks for AM using the DIW technique.

An electrically conductive polymer matrix composite can be developed by loading graphite particles in an aqueous CMC matrix. The non-Newtonian rheology of the CMC matrix shall enable the composite to be deposited using a DIW nozzle and the graphite particle will induce electrical conductivity. The development of the graphite-based electrically conductive polymer matrix composite is discussed in chapter 3.

The MARC multi-material robotic additive manufacturing setup has the ability to selectively deposit electrically conductive and insulating regions owing to the combination of the DIW and FFF tool heads. The selective deposition ability enabled the development of sensors, actuators, and hybrid systems which is presented in chapters 4 and 5.

2.3 Additive manufacturing using ceramic materials

Ceramic materials have various applications in mechanical, biomedical, and electrical domains owing to their hardness, corrosion resistance, thermal conductivity, and dielectric properties. Ceramics, however, are difficult to machine materials due to their high hardness and brittleness; therefore, they cannot be processed using conventional manufacturing techniques [27].

Ceramics parts are generally manufactured using slip casting where slurries are cast into molds and left to cure. The ceramic green body is then demolded and sintered in furnaces. The requirement of a mold greatly limits the design freedom as complex geometries are difficult to be demolded from conventional molds.

Additive manufacturing has disrupted the manufacturing sector due to its ability to manufacture complex geometries and application-specific parts without the need for expensive tooling. Concerted efforts have been made towards the additive manufacturing of ceramic materials. Ceramic materials can be processed using VAT polymerization,

material extrusion, powder bed fusion, and binder jetting techniques of additive manufacturing [28]. Ceramic powders with a particle size of less than 10 µm cannot be used in the binder jetting and powder bed fusion techniques and therefore, the processes result in high surface roughness, high porosity, and poor sintering densification. VAT polymerization on the other hand requires the ceramic powders to be transparent to the light source in order to facilitate polymerization. The requirement of transparency greatly limits the material that can be processed using VAT polymerization. The direct ink writing (DIW) variant of the material extrusion technique, however, utilizes highly loaded ceramic slurries with a minimum requirement of a binder, and therefore, highly densified ceramic bodies can be manufactured using this technique [29, 30].

The ability of direct ink writing (DIW) to deposit slurries enables additive manufacturing of ceramics. Feiden et al. demonstrated the DIW of aluminum oxide and silicon carbide ceramic slurries to produce highly dense ceramic bodies [31].

Rueschhoff et al. demonstrated the effects of the rheological properties of ceramic slurries on their printability and reported the maximum flexural strength of 156.6 MPa [32]. M'Barki et al. developed a mathematical model to gauge the additive manufacturability of ceramic slurry based on their rheological properties [33]. Yu et al. processed yttria-partially-stabilized zirconia ceramics through DIW [34]. Chan et al. demonstrated the effect of the rheological properties of clay on its printability and concluded that solid loadings above 55 vol% cause clogging of the nozzle however, solid loading below 35% yield poor shape retention.

Lopez et al. demonstrated the DIW of bioactive ceramic scaffolds for application in regenerative bone implants. The manufactured ceramics were tested in vivo in rabbits and bone regeneration was achieved [35].

Nan et al. demonstrated the DIW of borosilicate glass with high concentrations of alkali and alkaline oxide for the application in optics. However, the porosity retained by the sintered body resulted in the scattering of light and therefore, the obtained samples were opaque [36].

The literature reflects that DIW is a promising technique to manufacture parts from ceramics however, the rheological properties of the slurries play a key role in additive

manufacturability. The clogging of the deposition nozzle and the inability of the deposited slurry to bear the load of the subsequent layers is the bottleneck towards the manufacturing of complex geometries through DIW.

Lu et al. proposed a different approach towards slurry-based additive manufacturing of ceramics to produce complex geometries and named it negative additive manufacturing. Negative additive manufacturing involves the casting of the ceramic slurry into a sacrificial additively manufactured mold. The mold is later destroyed to obtain the ceramic green body [37].

The negative additive manufacturing technology enables the manufacturing of inexpensive molds in complex geometries. However, the technique relies on the flow of the slurry inside the mold which can prove to be difficult for slurries with high viscosity due to higher solid loading.

Wenbin et al. proposed a multi-material approach to improve the shape retention of ceramics by utilizing petrolatum, commonly known as petroleum jelly as a secondary support material. Petrolatum proved to be a viable support material and improve the shape retention in the manufactured parts; however, the rheology of petrolatum limits the load it could bear. Therefore, the number of layers that can be built on top of petrolatum is limited [38].

A multi-material deposition approach is proposed where the slurry is cast gradually into the mold as the mold is built up layer by layer. The multi-material approach is targeted to eliminate the voids left during the filling of the mold due to improper flow of the slurry. The MARC multi-material robotic additive manufacturing setup has the ability to selectively deposit PLA thermoplastic and ceramic slurry. The deposited PLA will act as the mold for the ceramic slurry. The multi-material additive manufacturing of ceramics is discussed in chapter 6.

Chapter 3

ELECTRICALLY CONDUCTIVE POLYMER COMPOSITES

3.1 Introduction

In this chapter, the development of CMC – graphite ePMCs is discussed. The ePMC inks are targeted for electrically conductive AM, and to eliminate the need to procure or synthesize an ePMC filament. The developed ePMCs are characterized using various characterization techniques. The effect of the concentration of graphite reinforcement on the rheology and electrical conductivity of ePMCs is discussed. The additive manufacturability of the ePMCs is qualitatively demonstrated. Furthermore, an application of an additively manufactured and electrically conductive part as a heating element was demonstrated.

3.2 Materials and methods

3.2.1 Materials

The chemicals used in this study are de-ionized (DI) water, sodium carboxymethylcellulose (CMC) with an average molecular weight of ~250,000 (Product# 419281, Sigma-Aldrich), and graphite powder (Product# 282863, Sigma-Aldrich). The average particle size of the graphite powder provided in the manufacturer's datasheet is 20 μm.

3.2.2 Synthesis of ePMC inks

ePMC inks were synthesized with various amounts of graphite loadings in two steps. In the first step, a 10 wt.% aqueous solution of CMC was prepared to be the matrix, by mixing CMC with DI water on a mechanical stirrer until homogenization. In the second step, the matrix was loaded with either 20 wt.%, 22.5 wt.%, or 25 wt.% graphite powder and mechanically stirred until homogenization. The ePMC inks were labeled 10CMC20, 10CMC22.5, and 10CMC25 respective to the amount of solid loading in them. Inks with loadings below 20 wt.% showed significant shrinkage after drying; therefore, these inks are not reported. Loading quantities above 25 wt.% were not pursued in this study because of the difficulty in homogenization during ink synthesis. A batch of matrix material without graphite (10CMC) was also retained to provide a baseline for characterization. In a typical ink combination, 3 g of CMC was mixed with 27 g of DI water to make the matrix, which was then loaded with 10 g of graphite powder. The ink was transferred to a pneumatic dispenser to be used for DIW.

3.2.3 Additive Manufacturing

A pneumatic DIW head mounted on a Mitsubishi Electric Melfa RV-2F robotic manipulator, as shown in Figure 3.1(a), was employed for additive manufacturing.

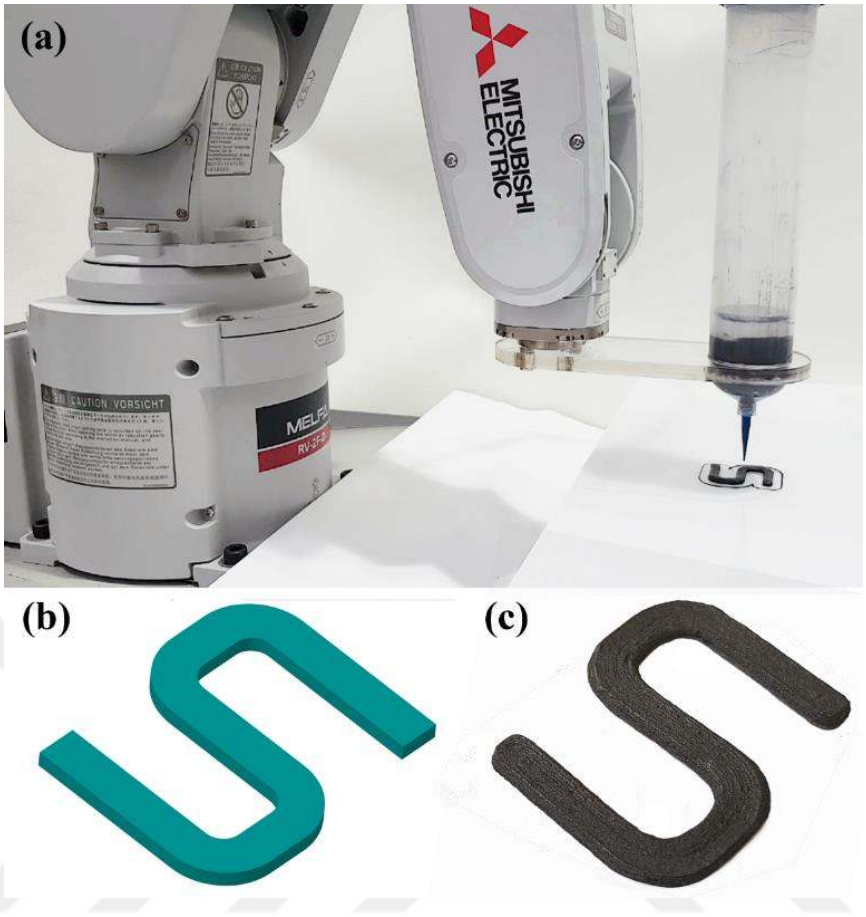

Figure 3.1. (a) Direct ink writing (DIW) head on a Mitsubishi Electric Melfa RV-2F robotic manipulator (b) CAD model of the electrical conductivity test specimen (c) Additively manufactured electrical conductivity test specimen.

The DIW head consisted of a 200 mL pneumatic dispenser with a tapered nozzle of 0.4 mm exit diameter. For the calibration of the inlet air pressure and nozzle speed, single lines of inks were deposited. Various air pressures and nozzle speeds were utilized at a fixed layer height of 0.3 mm to experimentally determine these important DIW process parameters for each ePMC ink.

Test specimens, as shown in Figure 3.1(b and c), were manufactured on poly(methyl methacrylate) (PMMA) substrates. The cross-sectional area of the test specimen was 10 mm^2 and the effective length of the conductive track was 100 mm. The process parameters obtained by the single line deposition tests, as reported in Table 3.1, were utilized for the manufacturing of the electrical conductivity test specimens. Seven test specimens were manufactured from each of the ePMC inks. The manufactured specimens were dried at room temperature for 24h.

Table 3.1. Direct ink writing process parameters for additive manufacturing of the electrical conductivity test specimens.

Label	Air Pressure (MPa)	Nozzle Speed (mm/s)
10CMC20	0.15	20
10CMC22.5	0.15	16
10CMC25	0.20	16

To qualitatively analyze the additive manufacturability of the material, scaffolds (25 mm x 25 mm x 10 mm) were additively manufactured using 10CMC20 ePMC ink. Rectilinear and honeycomb infill patterns were employed without changing the process parameters utilized during the AM of electrical conductivity samples.

3.3 Characterization

3.3.1 Composite characterization

The morphologies of 10CMC20, 10CMC22.5, and 10CMC25 were studied using a ZEISS Ultra Plus Field Emission Scanning Electron Microscope. The Fourier Transform Infrared (FT-IR) spectra were recorded with a Nicolet iS10 FT-IR Spectrometer, within the range from 4000 cm^{-1} to 650 cm^{-1} with a 2 cm^{-1} resolution. The samples for X-ray diffraction (XRD) were prepared by loading the graphite powder, CMC(neat) powder, and bulk 10CMC and ePMCs on a glass slide using double-sided carbon tape. X-ray diffraction analyses were performed on a Bruker D2 Phaser – X-ray Diffractometer with a Cu Kα1 radiation source using a wavelength of 1.54 Å and, a Lynxeye detector using a slit size of 1 mm. The power rating of the X-Ray generator was set to 30 kV at 10 mA current. The diffractograms were obtained within the 2θ range of 5˚ to 90˚ using a step size of 0.0204˚. The thermal degradation was analyzed on a TA Instruments Q500 model thermogravimetric analyzer using a platinum pan. After tarring, approximately 15 mg of each sample was placed in the pan and heated at a rate of 5 ˚C /min in N_2 within the range of 50 ˚C to 500 ˚C.

The rheologies of the inks were analyzed from 0.1 s^{-1} to 1000 s^{-1} at 20 ˚C on an Anton Paar MCR302 rheometer. A twin-gap geometry of 16 mm diameter with a compatible solvent trap was used at a gap of 0.339 mm. The evolution of viscosity and shear stress as a function of shear rate was recorded at a logarithmic spacing of 10 data points per decade.

3.3.2 Electrical Conductivity

The quantification of electrical conductivity is crucial for the development of ePMCs, to determine the electrical resistance of the final part. The resistances of test specimens were recorded using a Fluke 197 Digital Multimeter. The conductivity (κ) is given by

$$\kappa = \frac{l}{A} \times \frac{1}{R} \ (S.m^{-1}) \qquad \text{Eq. 3.1}$$

where R is the resistance (Ω), l is the length (m), and A is the cross-sectional area of the specimen (m^2).

3.4 Results and Discussion

3.4.1 Morphology

The morphologies of the three compositions of ePMCs (10CMC20, 10CMC22.5 and 10CMC25) are presented in Figure 3.2.

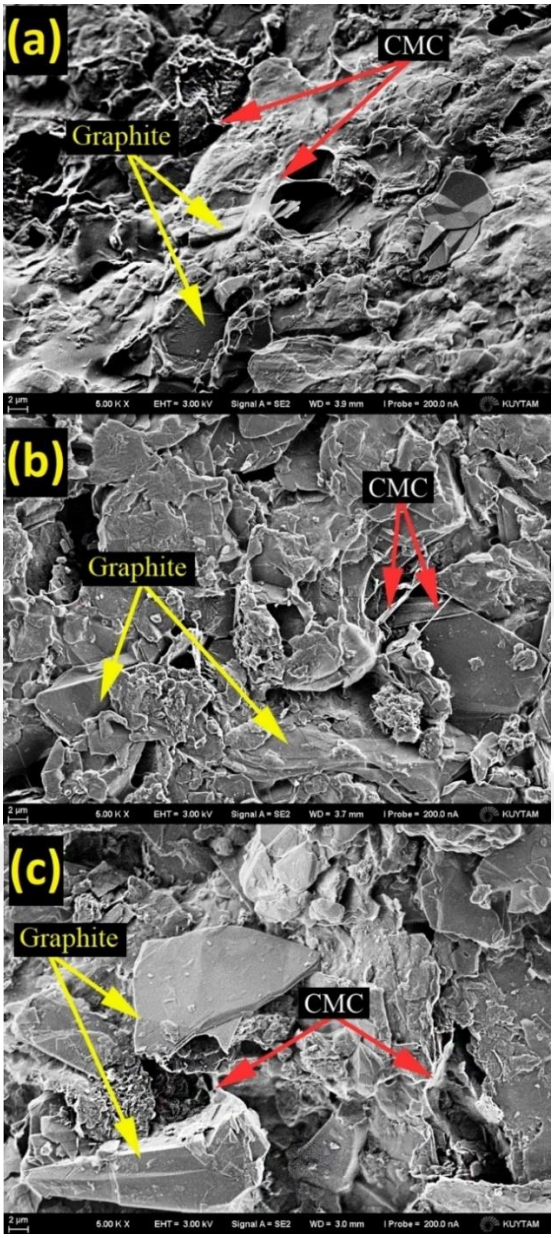

Figure 3.2. Scanning electron microscopy (SEM) images of (a) 10 wt.% aq. solution of CMC loaded with 20 wt.% graphite (10CMC20) (b) 10 wt.% aq. solution of CMC loaded with 22.5 wt.% graphite (10CMC22.5), (c) 10 wt.% aq. solution of CMC loaded with 25 wt.% graphite (10CMC25) after drying at room temperature for 24h.

Crystalline particles of graphite and polymeric strands of CMC are clearly visible. The graphite particles have formed continuous chains which act as electrical conduction paths. The polymeric strands of CMC hold the graphite chains together. In the absence of these strands, the graphite particles will not form a monolithic solid. As the graphite

loading in the ePMC increases, graphite particles become densely packed, increasing the graphite-graphite contact.

3.4.2 FT-IR Analysis

The FT-IR spectra of graphite, CMC(neat), 10CMC, and the three compositions of ePMCs are illustrated in Figure 3.3.

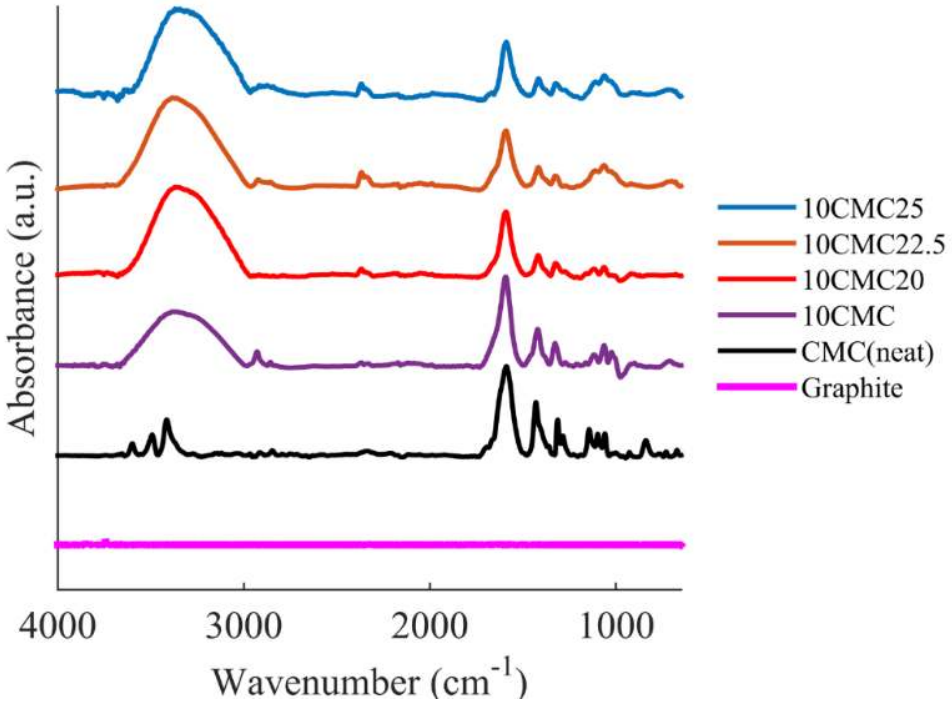

Figure 3.3. FT-IR spectra of graphite, CMC(neat) (as received CMC polymer), 10 wt.% aq. solution of CMC (10CMC), 10 wt.% aq. solution of CMC loaded with 20 wt.% graphite (10CMC20), 10 wt.% aq. solution of CMC loaded with 22.5 wt.% graphite (10CMC22.5), and 10 wt.% aq. solution of CMC loaded with 25 wt.% graphite (10CMC25) after drying at room temperature for 24h.

The FT-IR spectrum of graphite shows no significant absorption bands which infers the absence of any functional group. The spectrum of CMC(neat) shows an absorption peak at 1590 cm^{-1} which is attributed to the stretching vibration of the carboxylate group [39]. Strong absorption bands observed at 1420 cm^{-1} are attributed to -CH_2 scissoring vibration, while the band at 1320 cm^{-1} is attributed to -OH bending vibration [39]. Furthermore, the bands between 1000 cm^{-1} – 1100 cm^{-1} are attributed to C-O-C stretch vibrations [39]. Absorption peaks of -O-H stretch vibration was also observed between 3400 cm^{-1} – 3600 cm^{-1} [39]. The spectrum of 10CMC shows no significant change

compared to that of CMC(neat) except the conversion of multiple absorption peaks of O-H stretch vibration to a broad peak at 3365 cm^{-1}. The occurrence of this broad peak indicates the retention of trace amounts of water after drying. The spectra of the three compositions of ePMCs show no significant change compared to that of 10CMC; which suggests that there is no chemical interaction between graphite and 10CMC in the synthesis of ePMCs.

3.4.3 XRD Analysis

The X-Ray diffractograms of graphite, CMC(neat) (as received CMC polymer), 10CMC, and the three compositions of ePMCs are illustrated in Figure 3.4.

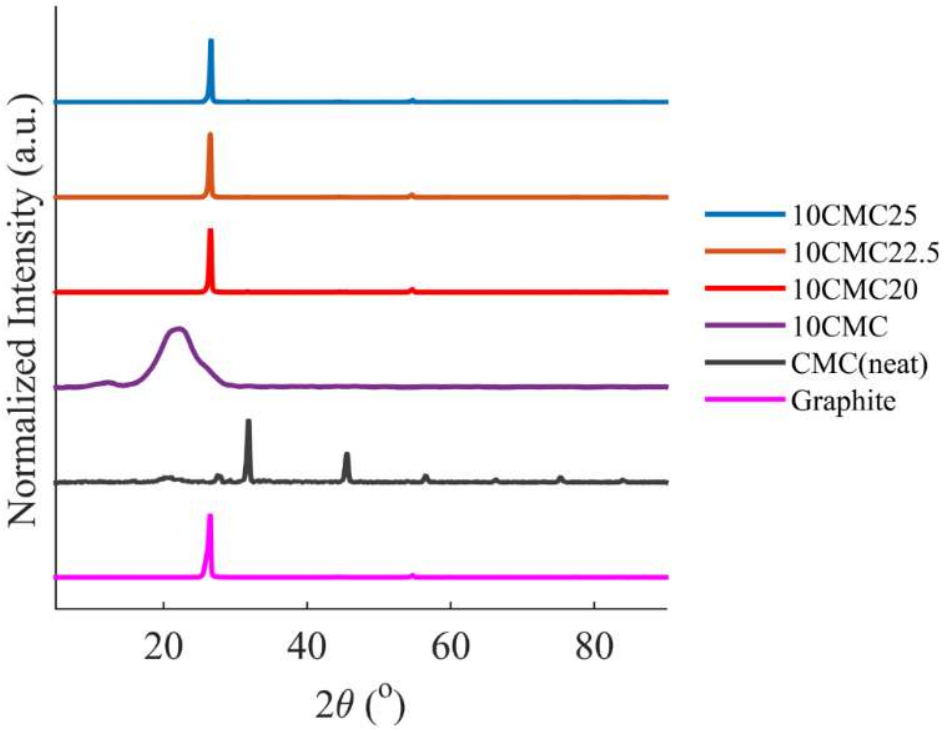

Figure 3.4. X-Ray diffractograms of graphite, CMC(neat) (as received CMC polymer), 10 wt.% aq. solution of CMC (10CMC), 10 wt.% aq. solution of CMC loaded with 20 wt.% graphite (10CMC20), 10 wt.% aq. solution of CMC loaded with 22.5 wt.% graphite (10CMC22.5), and 10 wt.% aq. solution of CMC loaded with 25 wt.% graphite (10CMC25) after drying at room temperature for 24h.

The characteristic peak of graphite is observed at 27˚ which corresponds to the Crystallography Open Database (COD) card number 9011577. Some sharp crystalline peaks are observed in CMC(neat) which disappear in 10CMC. This disappearance of

crystalline peaks in 10CMC and ePMCs along with the occurrence of a broad peak indicates that CMC loses its crystallinity after dissolution in water. The crystalline peaks of CMC(neat) were not analyzed further due to their absence in the ePMC inks. The recurrence of graphite peaks in ePMCs indicates retention of graphite's crystallinity and the absence of any chemical interaction. The peaks of graphite in the spectra of the ePMCs, overshadow the broad amorphous peak of 10CMC due to its low concentration in the composite. Therefore, this broad peak does not reappear in ePMCs.

3.4.4 Thermogravimetric Analysis (TGA)

The TGA scans of CMC(neat), 10CMC, and the three compositions of ePMCs are illustrated in Figure 3.5.

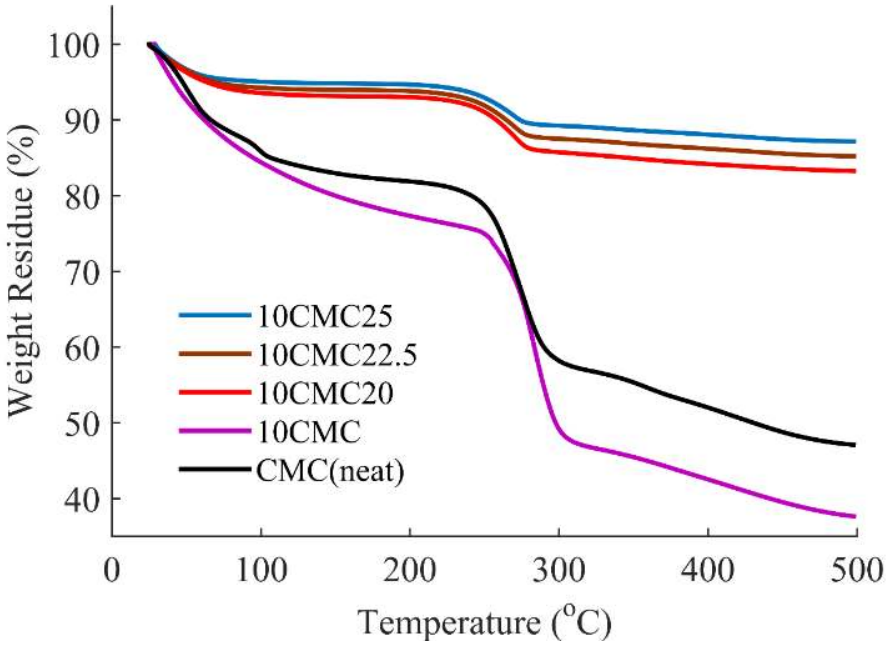

Figure 3.5. Thermogravimetric analysis (TGA) scans of CMC(neat), 10 wt.% aq. solution of CMC (10CMC), 10 wt.% aq. solution of CMC loaded with 20 wt.% graphite (10CMC20), 10 wt.% aq. solution of CMC loaded with 22.5 wt.% graphite (10CMC22.5), and 10 wt.% aq. solution of CMC loaded with 25 wt.% graphite (10CMC25) after drying at room temperature for 24h.

The reduction in weight residue at temperatures up to 100 ˚C for all tests is attributed to the loss of the retained moisture. The weight residues of CMC(neat) and 10CMC drop rapidly between 250˚C and 300˚C. This weight reduction is attributed to the conversion of the carboxyl group (-COO) to CO_2.

All three ePMC combinations display decomposition between 225 ˚C and 275 ˚C. This slight reduction in the decomposition temperature is attributed only to the presence of graphite as there is no chemical change in CMC. The conduction of heat to the CMC molecules in ePMCs is quicker due to the high thermal conductivity of graphite. Therefore, the activation energy required for the decomposition of the carboxyl group is achieved at slightly lower temperatures. The TGA scans indicate that the parts additively manufactured by the ePMCs inks will be thermally stable below 225 ˚C.

3.4.5 Rheology

The evolution of viscosity and shear stress as functions of shear rate for 10CMC and the three ink combinations are illustrated in Figure 3.6 and Figure 3.7.

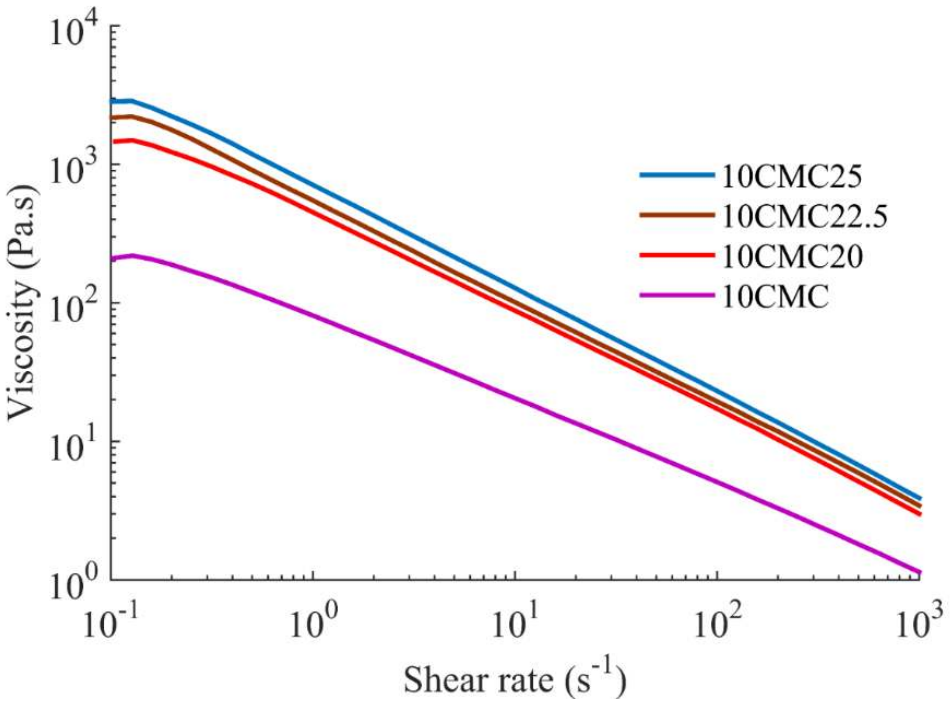

Figure 3.6. Viscosity versus shear rate flow curves of 10 wt.% aq. solution of CMC (10CMC), 10 wt.% aq. solution of CMC loaded with 20 wt.% graphite (10CMC20), 10 wt.% aq. solution of CMC loaded with 22.5 wt.% graphite (10CMC22.5), 10 wt.% aq. solution of CMC loaded with 25 wt.% graphite (10CMC25).

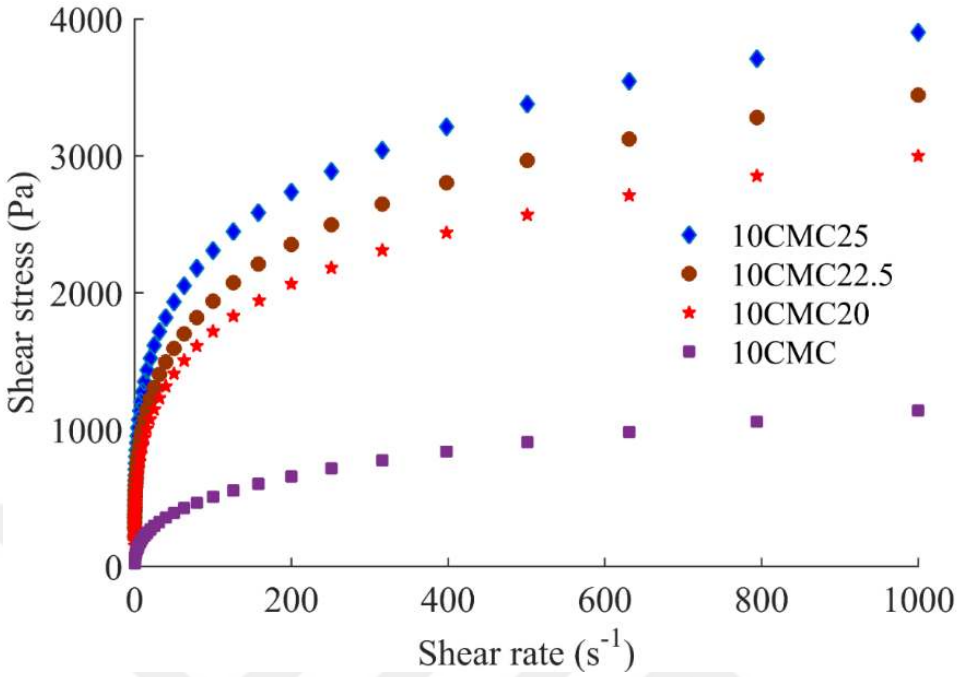

Figure 3.7. Shear stress versus shear rate flow curves of 10 wt.% aq. solution of CMC (10CMC), 10 wt.% aq. solution of CMC loaded with 20 wt.% graphite (10CMC20), 10 wt.% aq. solution of CMC loaded with 22.5 wt.% graphite (10CMC22.5), 10 wt.% aq. solution of CMC loaded with 25 wt.% graphite (10CMC25).

The non-Newtonian (shear thinning) of the aqueous solution of CMC which is attributed to the disentanglement of polymer chains of CMC [40] is retained in the ePMC inks.

The viscosities and shear stresses of the inks increase as the solid loading increases. This increase is attributed to the particle-polymer interactions in the ink. As the solid loading increases, the number of particle-polymer interactions increases. The friction of the particle-polymer interface induces resistance to the flow of ink increasing the viscosity and shear stress of the ink.

The rheology of ink plays a vital role in determining its usability in DIW. The maximum shear rate ($\dot{\gamma}$) during the DIW process can be calculated using the following relation [32]:

$$\dot{\gamma} = \frac{4Q}{\pi r^3} \qquad \text{Eq. 3.2}$$

where Q is the volumetric flow rate of the ink and r is the radius of the nozzle. The calculated max shear rate during DIW process for 10CMC20 is 388 s^{-1} and 312 s^{-1} for both 10CMC22.5 and 10CMC25. These shear rates correspond to a viscosity of 7 Pa.s – 10 Pa.s. Such low levels of viscosity during material deposition facilitate the material flow through the nozzle. After deposition, the viscosity of the deposited material increases two orders of magnitude. This increase in viscosity and shear stress facilitates the shape retention in the deposited material. It can be concluded that the rheological properties of the ePMC inks are suitable for AM using the DIW technique.

3.4.6 Electrical Conductivity of Additively Manufactured Specimens

The electrical conductivities of ePMCs as a function of graphite loading are presented in Figure 3.8.

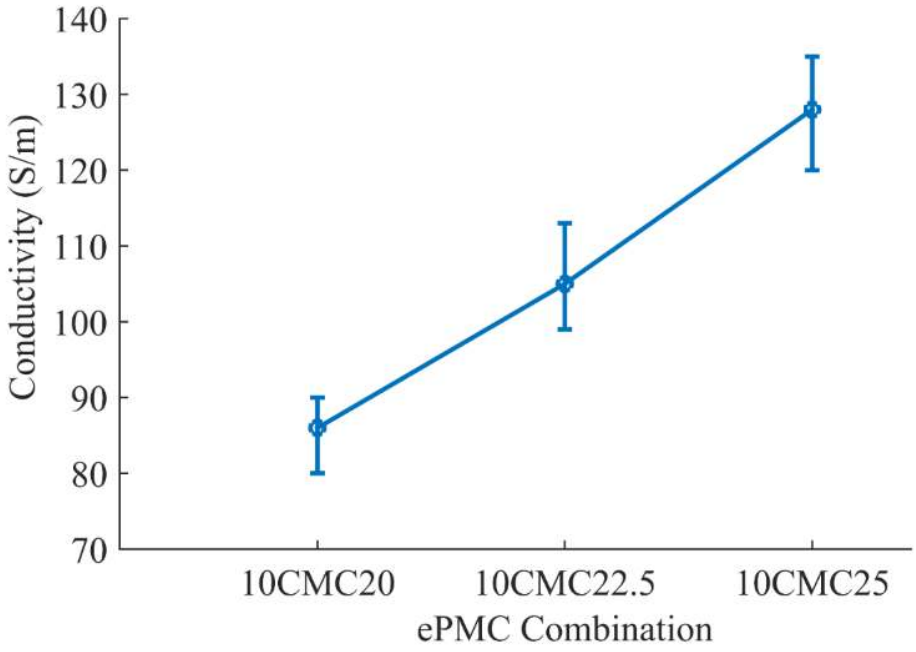

Figure 3.8. The electrical conductivities of 10 wt.% aq. solution of CMC loaded with 20 wt.% graphite (10CMC20), 10 wt.% aq. solution of CMC loaded with 22.5 wt.% graphite (10CMC22.5), and 10 wt.% aq. solution of CMC loaded with 25 wt.% graphite (10CMC25) after drying at room temperature for 24h.

It is observed that the conductivity of ePMCs increases linearly with the increase in graphite loading, within the studied range. As the graphite loading increases, the number of conductive chains in the ePMC increases which increases the conductivity. The results suggest that the tested loadings of graphite are well above the percolation threshold. The electrical conductivities of 87 – 128 $S.m^{-1}$ lie within the range of electrical conductivity (10^{-2} – 10^{3} $S.m^{-1}$) of various electrically conductive polymers and ePMCs reported by Kaur et al. [41].

The error between multiple test runs of the same ink combination is up to 15%. The electrical conductivity of powders is less than that of bulk material, as the interface between particles induces extra resistance to the flow of current [42]. The electrical conductivity of graphite is maximum parallel to its basal plane. During the synthesis of ePMC inks, the powders were mixed randomly therefore, the conduction path is random and cannot be categorized as perpendicular or parallel to the basal plane. The random orientation of graphite particles and the presence of water molecules are the main cause of the error observed between multiple test runs.

Electrical conductivities of the developed ePMCs lies in the moderate region of ePMCs being utilized in AM currently. The electrical conductivity is less than the ePMC filaments loaded with metallic reinforcements [14, 23]. However, heating the filaments for deposition through an FFF nozzle increases the changes of oxidation of metallic particles and disturbs the homogenization of the composite, which leads to unpredictability of the final resistance of the manufactured part. The electrical conductivity of additively manufactured specimens was characterized instead of the bulk ePMC filament to provide better predictability of the final resistance of the additively manufactured part. The electrical conductivity is significantly higher than the graphene-based ePMCs reported by Wei et al. [13] and the CNT-based composites reported by Farahani et al. [18] the commercially available ePMC filament marketed by ProtoPlant [21]. The developed ePMCs are also comparable to and Black Magic 3D [22]. The electrical conductivity of ePMCs is suitable for applications such as electrodes of ESDs as reported in [15]. The developed ePMCs eliminates the need for a pre-formed filament which reduces the cost of achieving selective electrical conductivity with AM.

3.4.7 Additive manufacturing

Figure 3.9 shows the scaffolds additively manufactured by the deposition of 10CMC20.

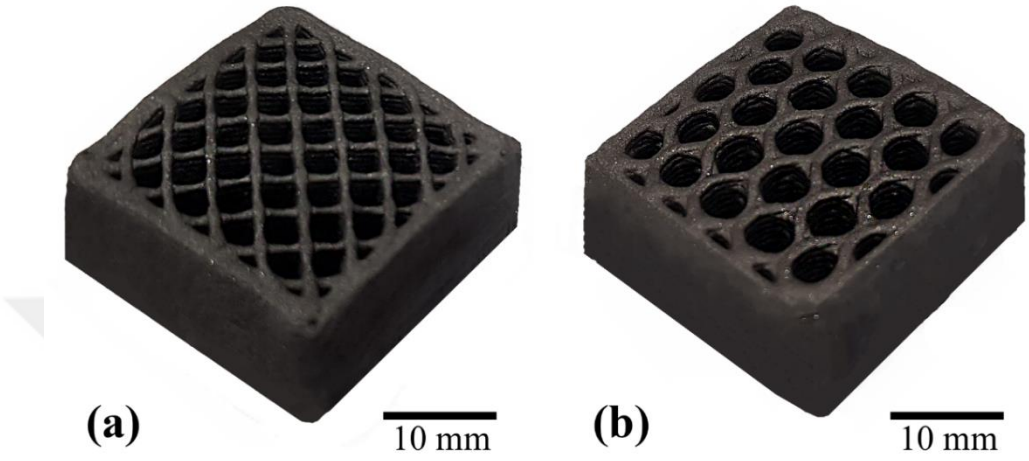

Figure 3.9. (a) Rectilinear infilled scaffold (25 mm x 25 mm x 10 mm) additively manufactured by the deposition of 10 wt.% aq. solution of CMC loaded with 20 wt.% graphite (10CMC20). (b) Honeycomb infilled scaffold (25 mm x 25 mm x 10 mm) additively manufactured by the deposition of 10 wt.% aq. solution of CMC loaded with 20 wt.% graphite (10CMC20).

The ink flows smoothly from the nozzle and can withstand the load of the subsequent layers. It can be concluded that 10CMC22.5 and 10CMC25 ePMC inks will be able to withstand the load of the subsequent layers, due to the higher viscosity and shear stress at low shear rates of these inks. The additively manufactured scaffolds demonstrate the usability of the ePMCs in AM to produce various conductive structures that can be difficult to produce via conventional manufacturing processes. The developed ePMC inks can be employed to additively manufacture structured electrodes for various applications in electrochemistry such as supercapacitors [43].

3.4.8 Homogeneity after Additive Manufacturing

To study the homogeneity of the ePMCs after AM, SEM micrographs of the three ePMCs were obtained at various positions. The SEM micrographs of the ePMCs after AM are illustrated in Figure 3.10.

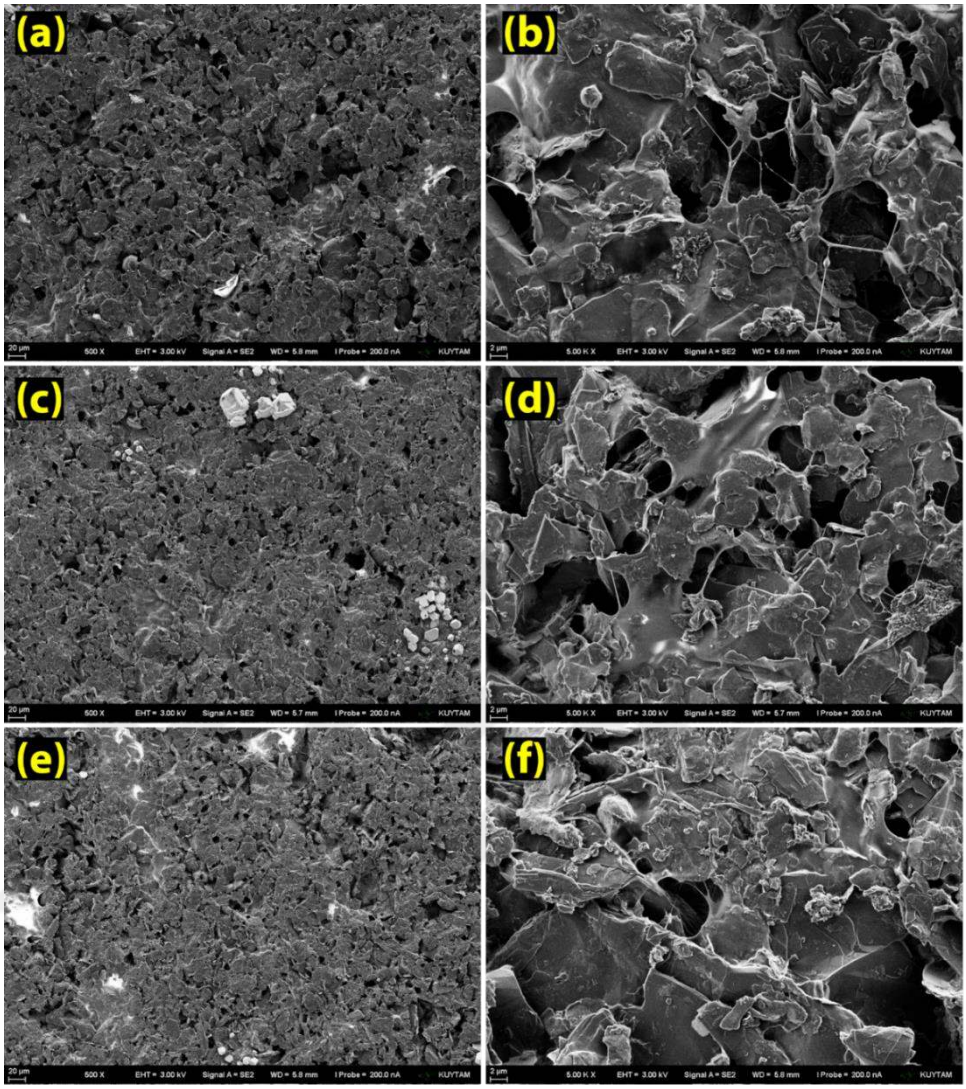

Figure 3.10. Scanning electron microscopy (SEM) images of additively manufactured specimen made from (a) 10 wt.% aq. solution of CMC loaded with 20 wt.% graphite (10CMC20) at x500 magnification, (b) 10CMC20 at x5000 magnification, (c) 10 wt.% aq. solution of CMC loaded with 22.5 wt.% graphite (10CMC22.5) at x500 magnification, (d) 10CMC22.5 at x5000 magnification, (e) 10 wt.% aq. solution of CMC loaded with 25 wt.% graphite (10CMC25) at x500 magnification, and (f) 10CMC25 at x5000 magnification after drying at room temperature for 24h.

The distribution of the graphite particles appears to be homogenous with the absence of any large voids at various locations in the ePMCs. To further ensure the homogeneity in the material, the 10CMC25 ePMC sample was subjected to an energy-dispersive X-ray spectroscopy (EDX) analysis. Due to the presence of carbon in both the constituents of ePMC, only the presence of oxygen was mapped. The EDX map of 10CMC25 is illustrated in Figure 3.11.

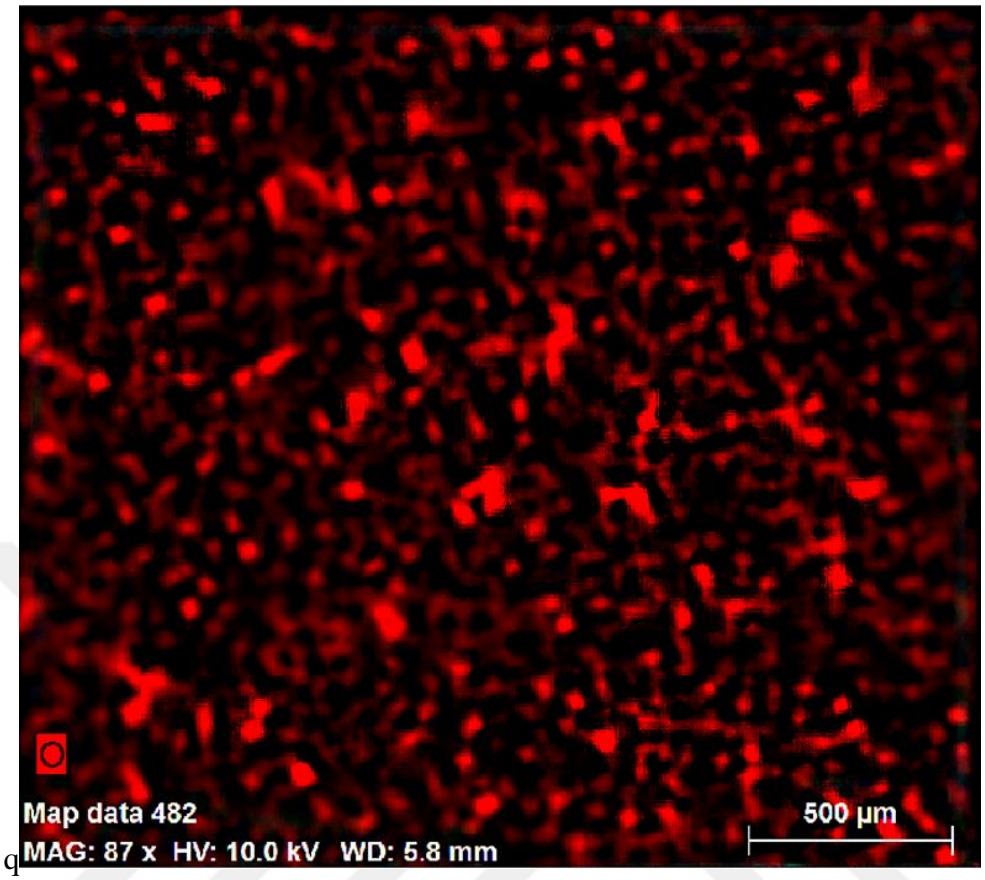

q

Figure 3.11. Energy-dispersive X-ray Spectroscopy map of oxygen in the 10 wt.% aq. solution of CMC loaded with 25 wt.% graphite (10CMC25) after drying at room temperature for 24 hours.

The EDX map shows a homogenous distribution of oxygen throughout the sample. Some clusters of oxygen can be seen, but these clusters are homogeneously distributed throughout. Therefore, from the SEM micrographs and EDX map, it can be concluded that the constituents of the ePMCs remain homogeneously distributed after AM.

3.5 Applications

The additively manufacturable ePMCs find various applications in the additive manufacturing of functional parts. The ePMC can be used to make circuits inside an additively manufactured part for the routing of current and signals. The moderate electrical conductivity of the ePMCs allows for the development of additively manufactured heating elements for application-specific geometries. Furthermore, electrically conductive structures can be manufactured to act as electrodes for the capacitive sensor.

This chapter discusses the development and additive manufacturing of sensors and heaters for various applications using the ePMCs.

3.5.1 Application for deicing

The developed ePMCs can be employed in applications where heating is required such as deicing. Application-specific heating elements of customized geometries can be embedded in additively manufactured parts as well as conventionally manufactured parts. To demonstrate a potential application of deicing using electrically conductive AM, a heating element with a mesh grid geometry was additively manufactured on a 7 mm thick carbon fiber reinforced polymer (CFRP) sheet. The 10CMC25 was used along with the process parameters reported in section 2.3.2. The geometry of the heating element was designed to have a resistance of 8 Ω; however, the resistance of the manufactured heating element turned out to be 8.57 Ω, drawing 1.4 A at 12 V. The additively manufactured heating element and a schematic of the de-frosting experiment are illustrated in Figure 3.12.

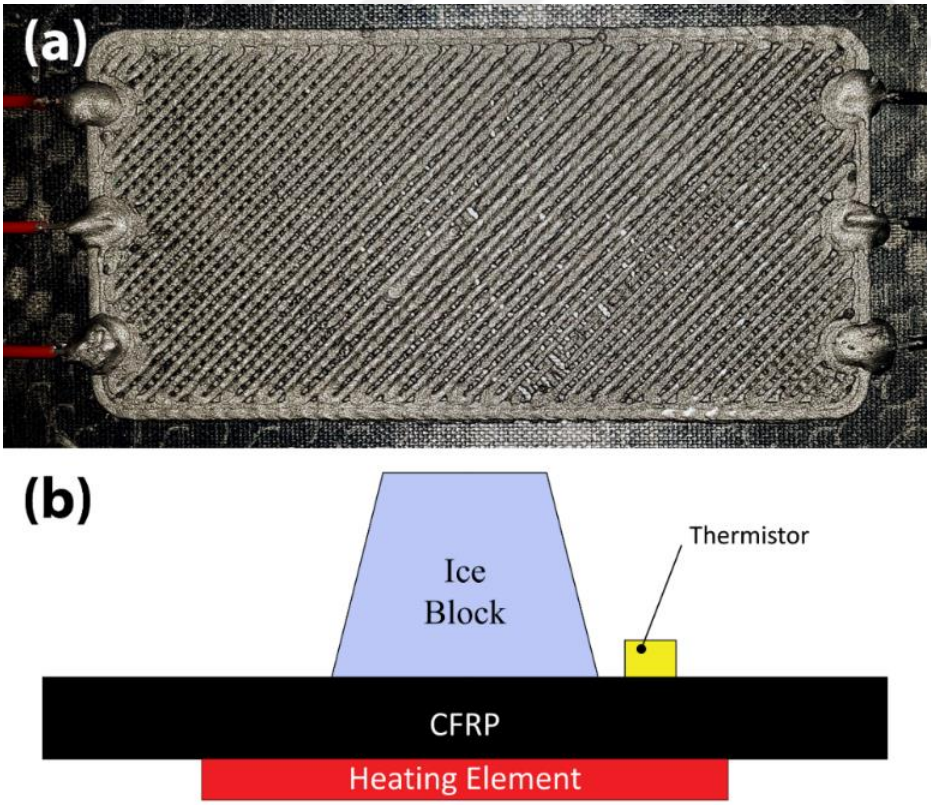

Figure 3.12. (a) Additively manufactured heating element (90 x 40 x 2 mm^3) with a resistance of 8.57 Ω. (b) Schematic of the de-frosting experiment.

A block of ice was placed on the opposite side of the CFRP sheet to simulate frosting and the heating element was turned on. A thermistor was employed to record the temperature of the CFRP-ice interface. The temperature of the CFRP-ice interface with and without heating is illustrated in Figure 2.13.

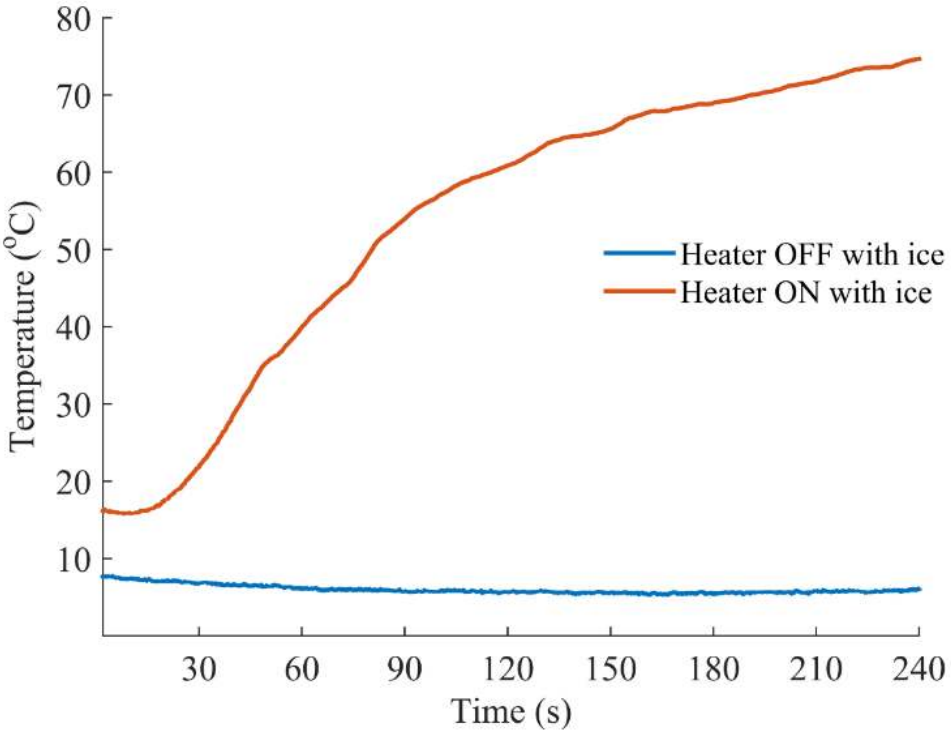

Figure 3.13. The temperature of the CFRP-ice interface during a de-frosting experiment with and without heating.

The increase in temperature of the CFRP-ice interface demonstrates the suitability of additively manufactured parts as heating elements. Customized heating elements can be conformally manufactured on free-formed surfaces, such as aerofoils, using suitable manipulators and multi-axis AM tool path algorithms [44, 45].

3.5.2 Development of capacitive sensors

The ePMCs can be used to develop capacitive sensors owing to their electrical conductivity. The capacitive sensing technique utilizes two oppositely charged electrodes. The surroundings of the electrodes act as a dielectric material. The schematic of a parallel plate capacitor is illustrated in Figure 3.14.

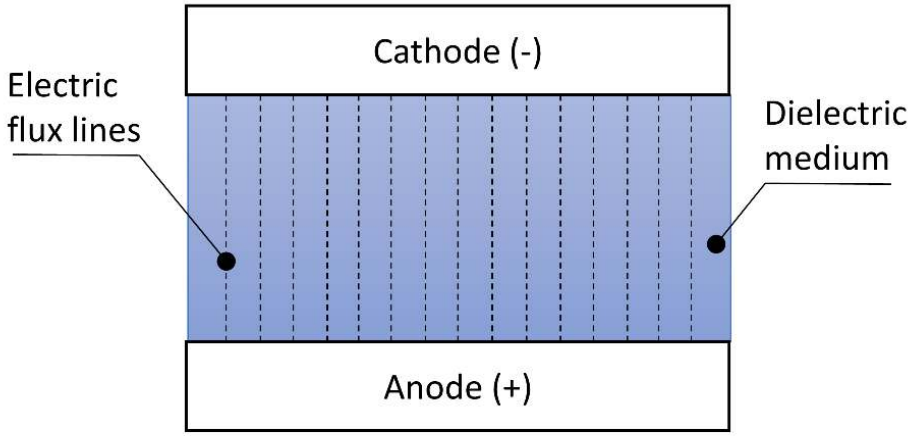

Figure 3.14. Schematic of a parallel plate capacitor.

The capacitance (C) of a parallel plate capacitor is given by

$$C = \varepsilon_o \times \varepsilon_r \times A/d \qquad \text{Eq. 3.3}$$

where, ε_o is the permittivity of vacuum, ε_r is the relative permittivity of the dielectric medium, A is the surface area of the electrodes and d is the distance between the two electrodes.

Capacitive sensors work on the principle of change in the relative permittivity of the surroundings as a result of an external agent such as frost, humidity, and human touch. The change in the relative permittivity of the surroundings changes the capacitive of the system. The change in the capacitance of the system results in the change in the resonance frequency of the circuit which is detected and recorded using a frequency to digital converter (FDC).

The additively manufacturable ePMC can be utilized to develop application-specific capacitive sensors. The flexibility of additive manufacturing enables the realization of complex and customizable geometries that cannot be manufactured using conventional manufacturing techniques.

3.5.3 Development of sensor and actuator hybrids

The application of ePMC as a heater discussed in section 3.5.1 and as capacitive sensors discussed in section 3.5.2 and be combined to develop a sensor and actuator

hybrid system. A control switch enables the hybrid system to shift from the sensing mode to the heating mode. when the control switch is in the normally open position no current passes through the system and therefore, the system acts as a capacitor. However, closing the control switch caused the current to pass through the system and therefore, the system acts as a resistive heater. The schematic of switching between capacitive sensing and resistive heating modes is illustrated in Figure 3.15.

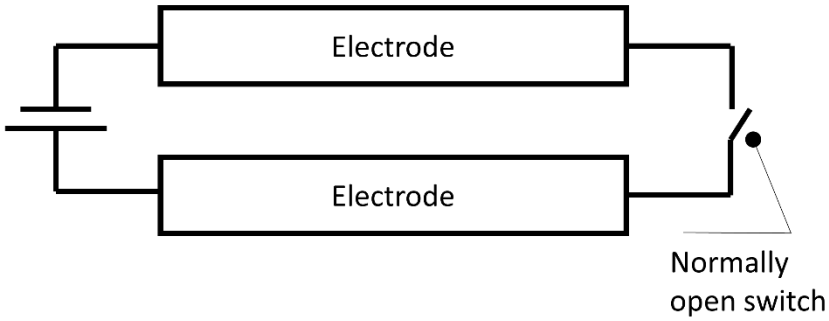

Figure 3.15 The schematic of switching between capacitive sensing mode and resistive heating mode.

A hybrid system for the detection of frost and defrosting was developed as a collaborative work, details of which can be found in the article Malik et al. [46].

3.6 Summary

New additively manufacturable and electrically conductive graphite-polymer composites were developed and characterized in detail. The electrical conductivity can be tuned in the range of 87 – 128 $S.m^{-1}$ depending on the amount of graphite loading. The FT-IR and XRD analyses confirm the absence of chemical interactions between constituents of the ePMC. The absence of any chemical interaction indicates that no hazardous by-products are produced during ink synthesis. The ePMCs can be employed in applications where the temperature is not expected to rise beyond 225 ˚C. The non-Newtonian shear-thinning rheology with low shear rate viscosity in the order of 10^3 Pa.s enables the ePMC inks to bear the load of the subsequent layers. Additively manufactured scaffolds and the homogeneity of the inks after AM demonstrate the employability of the developed ePMCs for electrically conductive AM. Electrically conductive tracks and structures of desired resistances can be additively manufactured without the need for an electrically functionalized pre-formed filament. Thus, reducing the cost and complexity

involved with achieving selective electrical conductivity with AM. Furthermore, an application of electrically conductive AM for the manufacturing of heating elements is presented. The developed ePMCs can be employed in diverse applications such as AM of conductive tracks, resistors, and electrodes for capacitors and energy storage devices. Virtuous to the low-cost and ready availability of graphite powder and CMC, the synthesis procedure is simple, up-scaleable, and cost-effective. Future efforts will include the adaptation of more efficient mixing regimes and finer particle-sized graphite powders to improve the electrical conductivities of the ePMCs.

Chapter 4

SMART DISINFECTION SYSTEM

4.1 Introduction

The severe acute respiratory syndrome coronavirus 2 (SARS-CoV-2) pandemic also known as COVID-19 has claimed the lives of more than 2 million people worldwide and is the biggest challenge to humanity since the second world war. The virus can either spread through direct human-to-human contact or exposure to contaminated surfaces. Studies indicate that the virus can survive up to 5 days on polymeric, metallic, and ceramic surfaces [47]. The incubation of the virus can be between 5 and 14 days however, pre-symptomatic shedding of the virus leads to the transmission by a pre-symptomatic carrier [48]. An average human involuntarily touches his mouth, nose, and eyes frequently, which increases the hazard of the transmission of the virus to and from common use surfaces [49]. Therefore, the common-use surface must be disinfected using a virucide [50]. The virucide methods include the use of soapy water, sodium hypo chloride, exposure to ultraviolet radiations, the exposure to heat.

The pandemic has severely affected all sectors of the industry compelling the adaptation of staggered working hours and frequent screening of symptoms for the workforce. However, a pre-symptomatic carrier might enter the workplace undetected which may lead to the exposure of the workforce to the virus. Furthermore, the use of common equipment such as toolboxes, equipment closets, and control panels may lead to

indirect transmission of the virus. The manual disinfection of common-use equipment after every user interaction cannot be guaranteed due to their frequency of use.

Various active disinfection systems have been reported in the literature for SARS-CoV-2. Murthy proposed a system for the disinfection of luggage using ultraviolet light [51]. Mahida et al. developed Tru-D^{TM}, an ultraviolet-based active disinfection device targeted for killing microorganisms in a confined space [52]. Yang et al. conducted an experimental study to validate the effectiveness of an ultraviolet-based Hyper Light Disinfection robot in eradicating different types of pathogens [53]. UV-irradiation has proven to be an effective virucide and can be employed to disinfect the equipment stored in closets. However, the hazardous nature of UV radiation limits their use in the disinfection of equipment during a work shift in the presence of personnel.

Thermal disinfection using heated chambers has also been implemented for decades and is being adapted in active disinfection systems targeted for SARS-CoV-2. An example of thermal disinfection of N95 facemasks has been reported [54]. Yu et al. reported thermal disinfection of air by utilizing heated nickel foams as air filters [55]. The engineers at Boeing are workings on a thermal disinfection prototype targeted for the disinfection of the difficult-to-reach areas of the flight deck [56]. The following are the recommended disinfection temperatures for the SARS-CoV-2 along with their respective exposure duration found in the literature [57, 58],

- 70ºC with an exposure of 5 minutes
- 75ºC with an exposure of 3 minutes
- 80ºC with an exposure of 1 minute.

Additive manufacturing offers design flexibility and enables the realization of application-specific geometries that cannot be produced by conventional techniques and materials [59]. The recent development of electrically conductive polymer composites for additive manufacturing has led to the development of additively manufacturable heating elements [60]. These heating elements can be additively manufactured in application-specific geometries for the localized disinfection of common-use equipment without the need for heated chambers. The common use equipment can be retrofitted with additively manufactured disinfection heaters however, the equipment cannot be constantly heated as temperatures above 55ºC are hazardous for humans to touch [61].

The handles of the common-use equipment are the potentially contaminated surfaces that users interact with. The available automatic disinfection solutions are inept to disinfect surfaces without human evacuation from the surroundings. Furthermore, neither of these systems can detect user interactions [51–55]. Therefore, smart disinfection systems are required which can detect user interactions and take disinfection measures accordingly without the need for a human evacuation from the surroundings. The equipment will be safe for the next user interaction once its temperature drops below 55ºC.

There are various touch and tactile sensors reported in the literature such as photoelectric sensors, piezoelectric sensors, and capacitive sensors [62, 63]. The capacitive sensing technique is widely implemented in various applications such as keypads, touch screens, prosthetics, and robotic arms [64, 65]. The capacitive sensors can therefore be adapted to detect user interaction with common-use surfaces. The additively manufactured heating elements owing to their electrical conductivity can serve a dual purpose of capacitive sensing electrodes. Therefore, the duality offered by the additively manufacturable sensor and heater can be utilized to develop a smart system that can detect user interactions and disinfect the common-use surfaces.

In this chapter, novel smart touch detection and disinfection system that employs an additively manufactured heating element that can function dually as a capacitive touch detection sensor is reported. The article reports the development of the system and its characterization along with its application on the door handles of closets.

4.2 Development of smart touch detection and disinfection system

The smart touch detection and disinfection system are implemented on a closet door handle that comprises an additively manufactured electrode that operates in dual mode. In the touch detection mode, the electrode is used to detect the touch of a human body on its surface whereas, in disinfection mode, the same electrode is used as a heating system. The switching between the touch detection mode and the disinfection mode is achieved through a control circuit. The LCD indicated the unsafe/safe-to-touch status of the door handle.

4.2.1 Additive manufacturing of the door handle

A combination of the fused filament fabrication (FFF) technique and the direct ink writing (DIW) technique was used to develop a multi-material additive manufacturing system, mounted on a Mitsubishi Electric robotic manipulator. The FFF head enables the deposition of polylactic acid (PLA) using a 0.3 mm nozzle, while the DIW head enables the deposition of electrically conductive polymer composites using a 0.4 mm nozzle. The combination of the FFF and DIW heads enables the selective deposition of electrically conducting and insulating regions in a single build. The preparation of the electrically conductive polymer composite having an electrical conductivity of 128 $S.m^{-1}$ is reported in our previous work [60]. Fig. 4.1(a) illustrates the multi-material additive manufacturing setup.

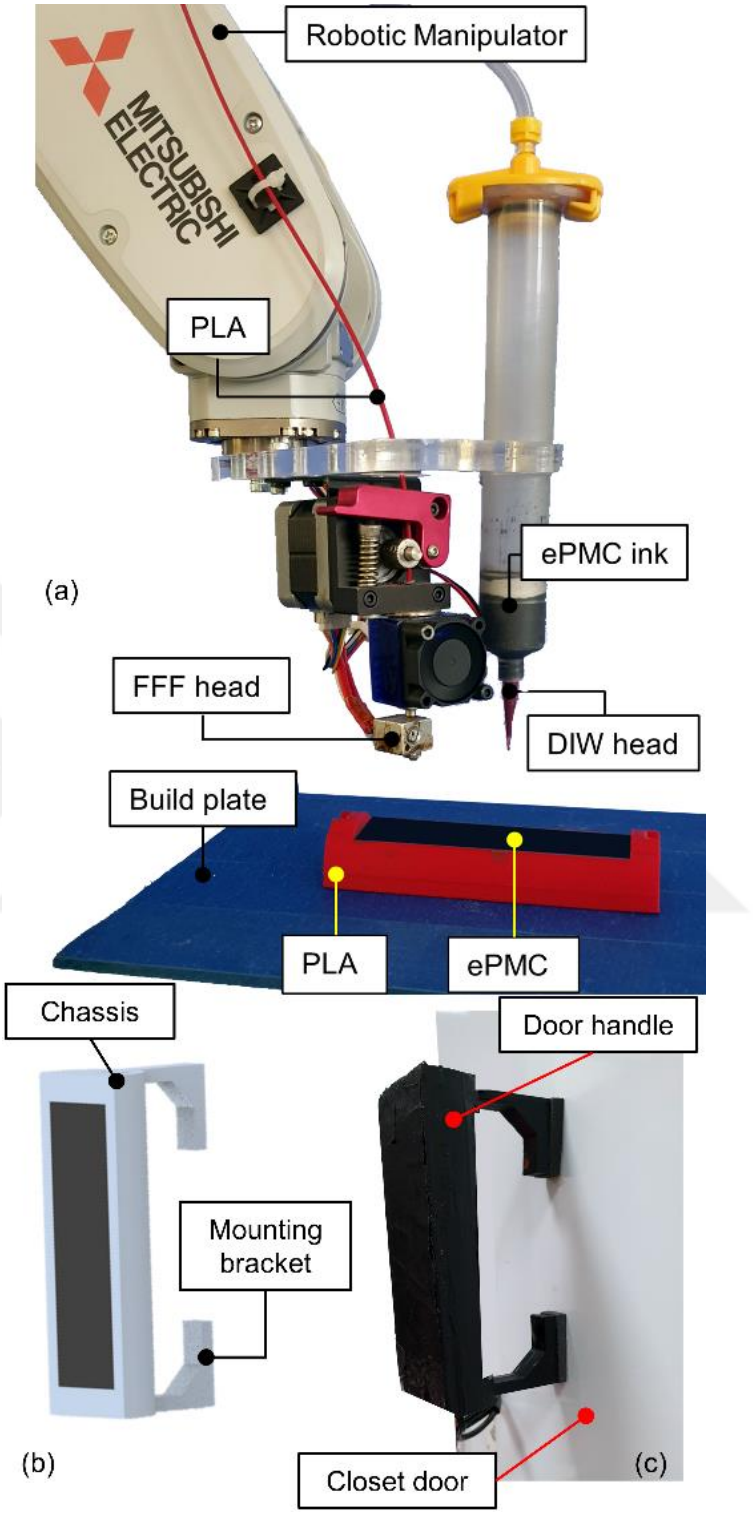

Figure 4.1. (a) The multi-material robotic additive manufacturing setup, (b) the CAD model of the handle, and (c) the smart disinfection system mounted on a closet door as a door handle.

The handle is additively manufactured using a multi-material robotic additive manufacturing setup. The handle is designed to be mounted using two additively

manufactured mounting brackets. The dimensions of the handle are kept in line with the anthropometric data for an adult hand having a grip length of 100 mm and a cross-section of 40 mm x 30 mm [66]. The chassis and the mounting brackets of the handle are manufactured from polylactic acid (PLA) using the FFF head while the embedded capacitive sensing electrode/ disinfection heater is manufactured from an electrically conductive polymer composite using the DIW head. The process parameters for multi-material additive manufacturing are tabulated in Table 4.1.

Table 4.1. Process parameters for the multi-material additive manufacturing of the smart disinfection system

Parameter	FFF Head	DIW Head
Nozzle diameter	0.3 mm	0.4 mm
Material	PLA	ePMC10CMC25
Build temperature	200°C	-
Layer height	0.2 mm	0.2 mm
Extrusion width	0.4 mm	0.4 mm
Linear speed	25 $mm.s^{-1}$	10 $mm.s^{-1}$
Infill pattern	Rectilinear	Rectilinear
Infill density	50%	100%
Top solid layers	2	2
Bottom solid layers	2	2
Perimeters	2	2

The handle was coated with graphite-loaded epoxy to ensure waterproofing before mounting on the closet door. The CAD model of the door handle is illustrated in Figure. 4.1(b) and the smart disinfection system mounted on a closet door is illustrated in Figure 4.1(c).

4.2.2 Touch detection mode

The touch detection system employed in this paper is based on the principle of capacitive sensing. The capacitive sensor is configured in a self-capacitance mode, where an additively manufactured electrode is subjected to an alternating voltage source. The

electric charge is stored on the surface of an electrode in the form of an electric field and is known as the self-capacitance of the electrode. The overall density of the electric field changes when the electrode interacts with the human body. This change in the electric field density is owed to the dielectric properties of the human body [67, 68]. The variation in the charge density with respect to the interacting external body brings a shift in the self-capacitance of the electrode [69]. This change in self-capacitance is used for touch detection. The electrode is attached in parallel with an inductor-capacitor (LC) resonating circuit that is driven by a commercially available frequency to digital converter (FDC). The LC resonator oscillates at a frequency of 40 MHz. The change in the self-capacitance of the electrode, consequent to the interacting human body varies the frequency of the LC resonator. Figure. 4.2 illustrates the schematics of the self-capacitance-based touch detection system.

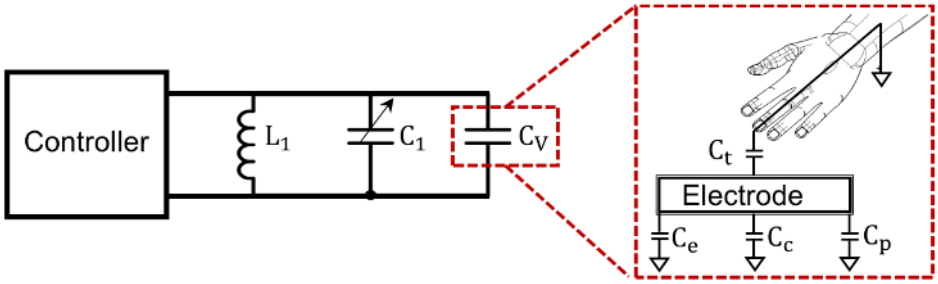

Figure 4.2. The schematic of the self-capacitance-based touch detection system.

The resonator is indicated by an inductor $L_1 = 10\mu H$ and a capacitor $C_1 = 39pF$, the variable capacitor C_v indicates a sum of the self-capacitance C_t between the electrode and the interacting human body, the parasitic capacitance C_p of the circuit, the capacitance C_e between the electrode and the ground and the capacitance C_c between the electrode and the electrical connections. The variation in the capacitances C_p, C_e, and C_c are negligible as compared to the self-capacitance C_t therefore they are assumed constant throughout the experiment. The self-capacitance C_t depends on various human factors such as the size, thickness, and the number of fingers in contact with the sensor.

The change in the self-capacitance of the electrode, consequent to the interacting human body varies the frequency of the LC resonator. This change in the frequency is measured by the FDC and is converted into equivalent capacitance using Equation 4.1.

$$F = \frac{1}{2\pi\sqrt{L_1 C}} \quad \text{Eq. 4.1}$$

where C is the equivalent capacitance of the whole system and is denoted by a summation of C_1 and C_v, illustrated in Equation 4.2.

$$C = C_1 + C_v \quad \text{Eq. 4.2}$$

The resonance frequency of the system decreases when it comes in contact with the human hand. The removal of the human hand from the capacitive circuit induces an increase in the resonance frequency. The changes in the resonance frequency of the system are adapted as the triggers for the detection of user interaction.

4.3 Disinfection mode

Electrical current is passed through the additively manufactured heating element in the disinfection mode. The temperature of the heating element is controlled by a proportional integral derivative (PID) controller that employs an NTC 100k thermistor for feedback. The heat (H) generated by the heating element is represented by the equation.

$$H = V\ I\ t \quad \text{Eq. 4.3}$$

where V is the voltage applied to the heating element, I is the current drawn by the heating element, and t is the heating duration. The voltage applied to the disinfection heater is controlled by the PID controller using pulse width modulation (PWM) and the current drawn is recorded by an ACS712 current sensor. The maximum power consumed by the heater is 25 W. The heater was characterized for its heating and cooling responses for the target temperatures of 70ºC, 75ºC, and 80ºC. The heater is passively cooled by the ambient air. The heating and the cooling responses of the system were utilized to tune the proportional, integral, and derivative gains of the PID controller.

4.3.1 Disinfection on-demand algorithm

An 8-bit microcontroller is used to integrate the touch detection mode, disinfection mode, and the LCD status indicator. The system starts in the touch detection mode and waits for user interaction while the LCD indicates the “Safe to touch” status. User

interactions with the door handles of closets vary from application to application. Typically, the user interactions with door handles of closets can be divided into either continuous contact interactions or interrupted contact interactions. In continuous contact interactions, the user maintains contact with the door handle while using the closet. On the other hand, the user touches the door handle at least twice while using the closet in case of interrupted contact interaction. Therefore, a dwell of 60 seconds has been added to the system where the system waits for a subsequent contact before determining the end of user interaction. The end of user interaction is determined if there is no subsequent user contact during the dwell time. The dwell time may be customized based on the application. The disinfection module is triggered at the end of a user interaction where the system is heated to the disinfection temperature followed by an isothermal hold. The LCD indicates the “Do not touch” status during the disinfection mode. The end of the disinfection mode reverts the system to the touch detection mode, while the LCD indicates “Do not touch” status till the temperature of the system drop below 55ºC which makes the system safe to touch, and the same is indicated by the LCD. The flowchart of the disinfection on-demand algorithm is illustrated in Figure. 4.3.

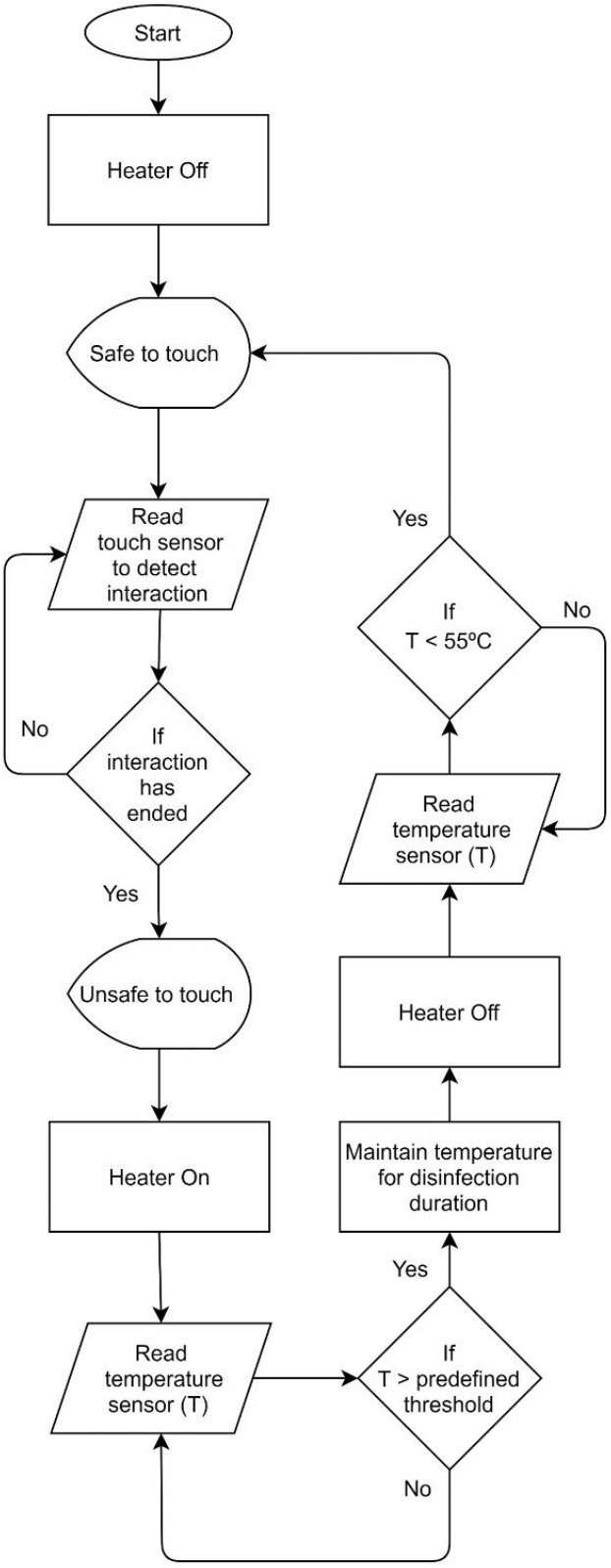

Figure 4.3. Flowchart of the disinfection on-demand algorithm.

4.4 Results and discussion

4.4.1 Characterization of the touch detection sensor

The response of the capacitive sensing module to human touch is illustrated in Figure. 4.4. The door handle is in contact with the surrounding air initially, and there is no significant change in the resonance frequency of the LC circuit. The user interaction with the surface of the door handle causes a sharp decrease in the resonance frequency due to the higher dielectric of the human hand as compared to that of air. This sharp decrease is reflected by the negative peak in the change in frequency trend. The change in frequency remains insignificant during the engagement. The resonance frequency increases when the human hand disengages the door handle which is recorded as an indication of the end of the user interaction. The subsequent peaks reflect the variations in the magnitude of the resonance frequency due to the difference in the grip type. The variations in the magnitude of change in frequency for various test subjects and grip styles are tabulated in Table 4.1. A ±40 kHz change in the frequency adapted as the threshold for the detection of a touch.

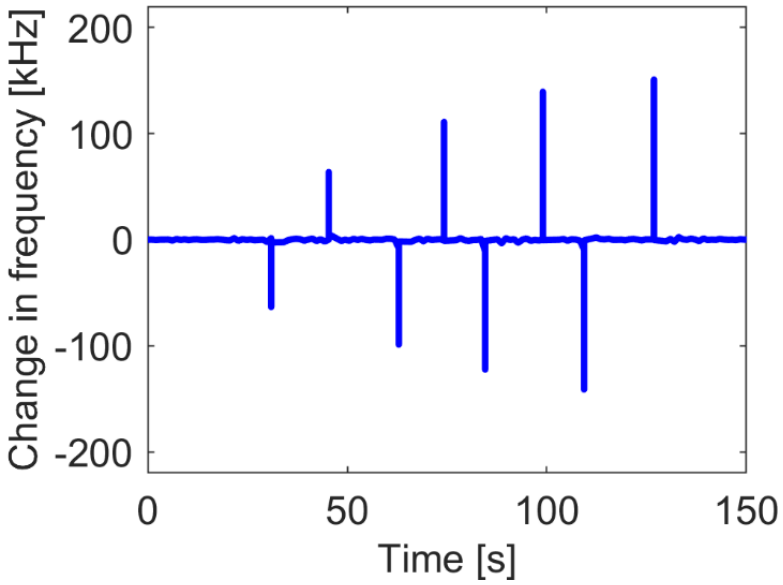

Figure 4.4. The response of the capacitive touch detection sensor for pinch grip (first pair of peaks), 2-finger claw grip (second pair of peaks), 3-finger claw grip (third pair of peaks), and 4-finger claw grip (fourth pair of peaks).

Table 4.2. The changes in the resonance frequency for various test subjects.

Test Subject	Change in frequency [kHz]			
	Pinch grip	2-finger claw grip	3-finger claw grip	4-finger claw grip
1	±96	±140	±174	±198
2	±62	±100	±118	±126
3	±64	±98	±122	±151

4.4.2 Characterization of disinfection heater

The disinfection heater was characterized at an ambient temperature of 20ºC. The response of the disinfection heater for the disinfection temperatures of 70ºC, 75ºC, and 80ºC is illustrated in Figure. 4.5. The rise time, hold time, and cooldown time along with the total energy consumption of the disinfection strategies are tabulated in Table 4.2. The results indicate that the three different disinfection strategies yield approximately the same cycle time. The total energy consumption is a function of both the rise time and the hold time. The increase in the disinfection temperature increases the rise time however, the requirement of isothermal hold at higher disinfection temperature is significantly reduced as discussed in section 4.1. Therefore, the energy consumption is expected to behave nonlinearly with the increase in disinfection temperature. The 70ºC is selected for the smart disinfection system owing to its lowest energy consumption. The energy consumption is expected to reduce further where room temperature is maintained above 20ºC.

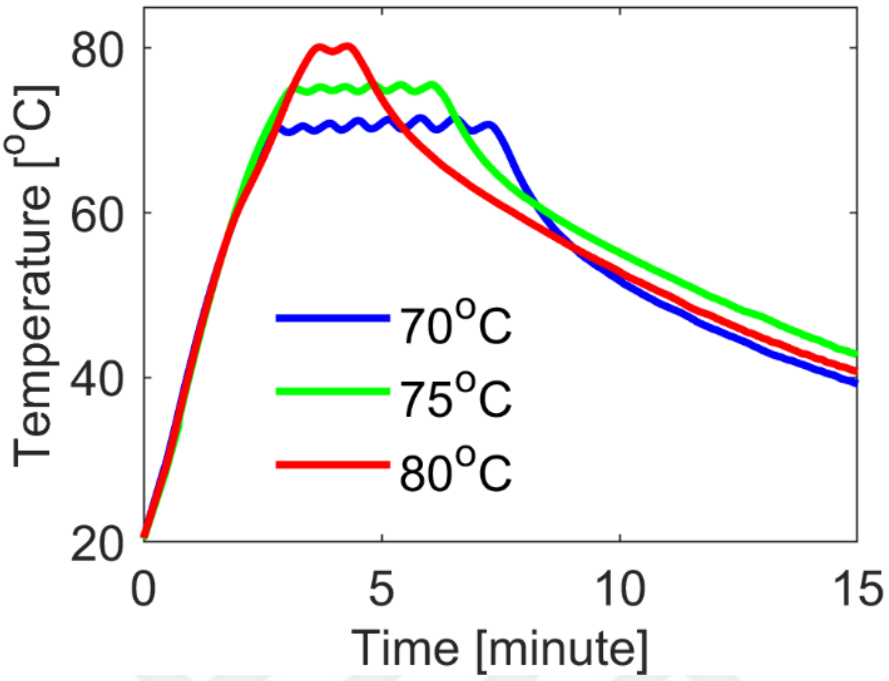

Figure 4.5. The evolution of the temperature of the door handle for 70ºC, 75ºC, and 80ºC disinfection strategies and their respective exposure times.

Table 4.3. The rise, hold, cooldown, and total cycle time of the 70ºC, 75ºC, and 80ºC disinfection strategies along with their respective energy consumption.

Disinfection temperature (ºC)	**Rise time (minute)**	**Hold time (minute)**	**Cooldown time (minute)**	**Total cycle time (minute)**	**Energy consumed (Wh)**
70	2.7	5	1.7	9.4	1.60
75	3.1	3	3.7	9.8	1.71
80	3.5	1	4.8	9.3	1.61

4.4.3 Disinfection on-demand

The integration of the sensing and disinfection module for the 70ºC disinfection strategy is illustrated in Figure 4.6. The system remains safe to touch (high) and becomes unsafe to touch (low) when user interaction is detected by the touch detection sensor. The controller detects the end of user interaction and performs the prescribed heating for

disinfection. The system becomes safe to touch and waits for the next user interaction after its temperature drops below 55ºC.

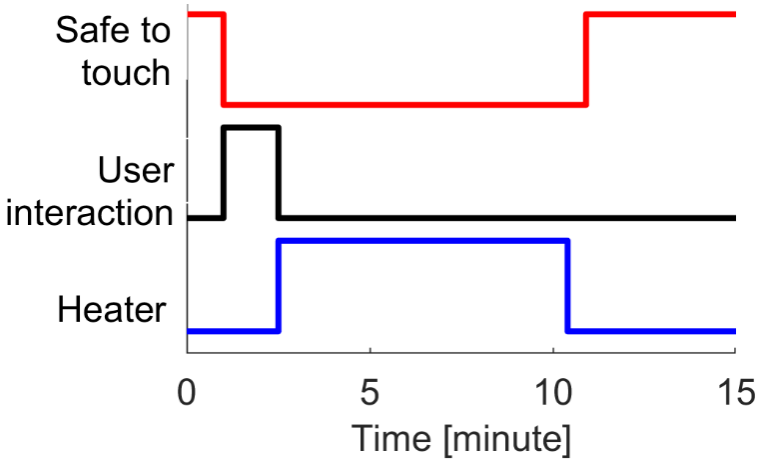

Figure 4.6. The digital response of the tough detection system for the 70ºC disinfection strategy.

4.4.4 Efficacy of the system

The ability to trigger disinfection measures based on the detection of user interactions enables the smart disinfection system to attenuate the indirect spread of the SARS-CoV-2. The smart disinfection system automatically disinfected the door handles at the cost of roughly 1.6 Wh of energy to prepare the equipment for the next user interaction. The automated disinfection significantly reduces the load on the janitorial staff and does not need human evacuation from the surroundings. The total cycle time of the system is 10 minutes approximately and is suited for applications where the expected number of interactions in an 8-hour work shift is less than 40. The additive manufacturability of the system enables the flexibility in design needed for the adaptation of the system for various industrial applications such as the handles of power tools, closet doors, refrigerator doors, and doors of control panels. The system is flexible and can be adapted for disinfection during the outbreak of diseases other than COVID-19. The limitation of the system is the passive cooling rate. The door handle might be at a temperature higher than 55ºC which may create the need to use a heat-resistant glove to open the closet in the case of an emergency. Active cooling can also be implemented to reduce the cooldown time.

4.4.5 Incorporation of active cooling

The disinfection cycle time can be further reduced by the incorporation of an active cooling system for applications with higher rates of user interactions at the cost of additional energy consumption. The reduction in the cooling time was investigated by the installation of two 40 x 40 x 10 mm^3 casing fans on the mounting brackets for forced convective cooling. The CAD model of the complete system along with the modified mounting brackets and the installed fans is illustrated in Figure. 4.7 (a).

Each of the installed casing fans operates at 0.5 W creating airflow of 164 liters per minute. The disinfection on-demand was modified to turn the cooling fans on at the end of the heating cycle. The cooling fans are triggered off when the temperature drops to room temperature. the increased cooling rate of the system in response to forced convective cooling is illustrated in Figure. 4.7 (b). The cooldown time is reduced to 1.5 minutes, 1.9 minutes, and 2.2 minutes for the 70ºC, 75ºC, and 80ºC, respectively.

The maximum reduction of 54% in the cooldown time is observed for the 80ºC disinfection strategy. This reduction in the cooldown time reduced the cycle time to approximately 7 minutes for the strategy. This reduction in the cycle time allows the system to be adopted in applications where the expected rate of user interactions is less than or equal to 65 user interactions in an 8-hour work shift.

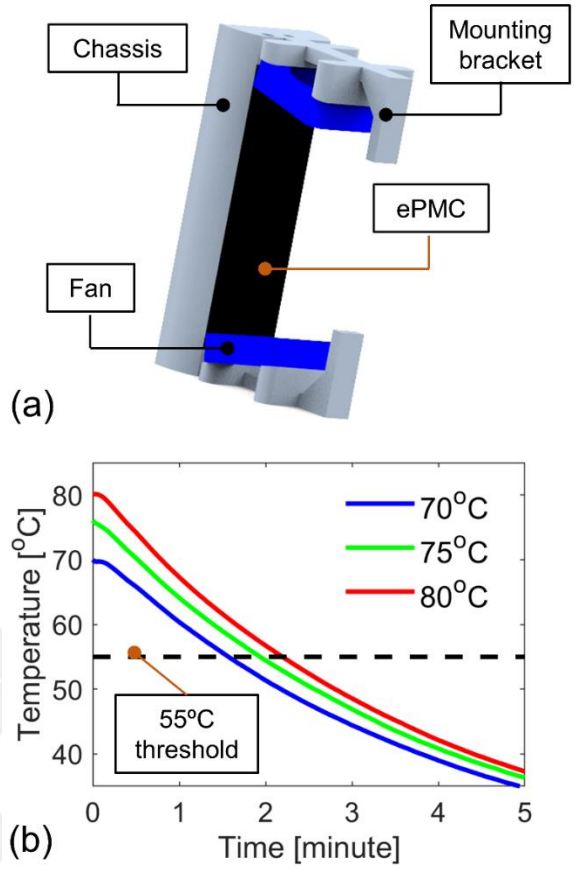

Figure 4.7. (a) CAD model for the implementation of the forced convection-based active cooling. (b) The active cooling response of the system from 70ºC, 75ºC, and 80ºC.

4.5 Conclusion

In summary, a novel smart touch detection and disinfection system target for the disinfection of surfaces potentially contaminated by SARS-CoV-2 was proposed. The system employs a low-powered and additively manufactured disinfection heater that serves a dual purpose of a capacitive touch sensor providing the feedback of user interaction. The response of the capacitive sensor was characterized for different types of hand grips and various disinfection strategies were tested. The thermal disinfection strategy of 5-minute exposure at 70°C was selected owing to its lower energy consumption of 1.6 Wh. The system becomes safe to touch when its temperature drops below 55ºC and the same is indicated by an LCD. The additive manufacturability of the system renders the system adaptable in various industrial applications where the expected user interactions are less than or equal to 40 interactions in an 8-hour work shift for a passively cooled system. The incorporation of active cooling using casing fans increases

the number of interactions to 65 for an 8-hour work shift. The system may also be adapted for the disinfection against outbreaks of contagious diseases other than SARS-COV-2.

Chapter 5

ADDITIVE MANUFACTURING OF CERAMICS

5.1 Introduction

The negative additive manufacturing technology enables the manufacturing of inexpensive molds in complex geometries. However, the technique relies on the flow of the slurry inside the mold which can prove to be difficult for slurries with high viscosity due to higher solid loading. A new multi-material deposition approach is proposed where the slurry is cast into the mold as the mold is built up layer by layer. The multi-material approach is targeted to eliminate the voids left during the filling of the mold due to improper flow of the slurry.

This chapter discusses the multi-material deposition approach for the additive manufacturing of ceramic bodies with highly loaded ceramic slurries to obtain dense ceramic parts with complex geometries.

5.2 Materials and methods

5.2.1 Materials

The chemicals used in this study are polylactic acid (PLA)((eSun), dichloromethane (DCM) de-ionized (DI) water, sodium carboxymethylcellulose (CMC) with an average molecular weight of ~250,000 (Product# 419281, Sigma-Aldrich), fine aluminum oxide (alpha, Molchem).

5.2.2 Preparation of ceramics slurry

Slurries were synthesized with various amounts of solid loadings in two steps. In the first step, a 5 wt.% aqueous solution of CMC was prepared to be the matrix, by mixing CMC with DI water on a mechanical stirrer until homogenization. In the second step, the matrix was loaded with the solid loading of 68.75 wt.% gradually and mechanically stirred until homogenization. The slurry was then transferred to a pneumatic syringe to be used in the multi-material additive manufacturing setup.

5.2.3 Ceramic part and mold geometries

Gyroid-based complex geometry and its negative mold were designed using the nTopology modeling software to demonstrate the potential of the multi-material deposition approach. The following Figure 5.1 demonstrates the target geometry and the negative mold.

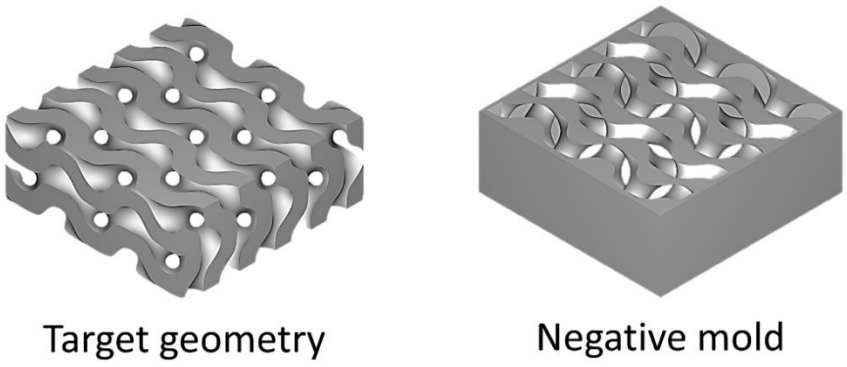

Figure 5.1. Target geometry and the negative mold.

5.2.4 Multimaterial additive manufacturing of ceramic green body and mold

The multi-material robotic additive manufacturing setup is illustrated in the following figure was utilized to manufacture the ceramic green body and the negative mold. The CAD data of the target geometry and the negative mold were assembled in the toolpath generation software CURA. The process parameters are tabulated in Table 5.1.

Table 5.1. Process parameters for the multi-material additive manufacturing of the molded ceramic green body.

Parameter	FFF Head	DIW Head
Nozzle diameter	0.3 mm	1.2 mm
Material	PLA	Al_2O_3 slurry
Build temperature	200°C	-
Layer height	0.2 mm	1 mm
Extrusion width	0.4 mm	1 mm
Linear speed	25 $mm.s^{-1}$	10 $mm.s^{-1}$
Infill pattern	Rectilinear	Rectilinear
Infill density	0%	100%
Top solid layers	2	2
Bottom solid layers	2	2
Perimeters	2	2

The FFF head builds the negative mold layer by layer with a layer height of 0.2 mm. The DIW head casts the ceramic slurry inside the mold once after every 5 layers of the mold have been deposited. The following Figure 5.2 illustrates the toolpath of two distinct layers. The samples were left to dry overnight at ambient conditions.

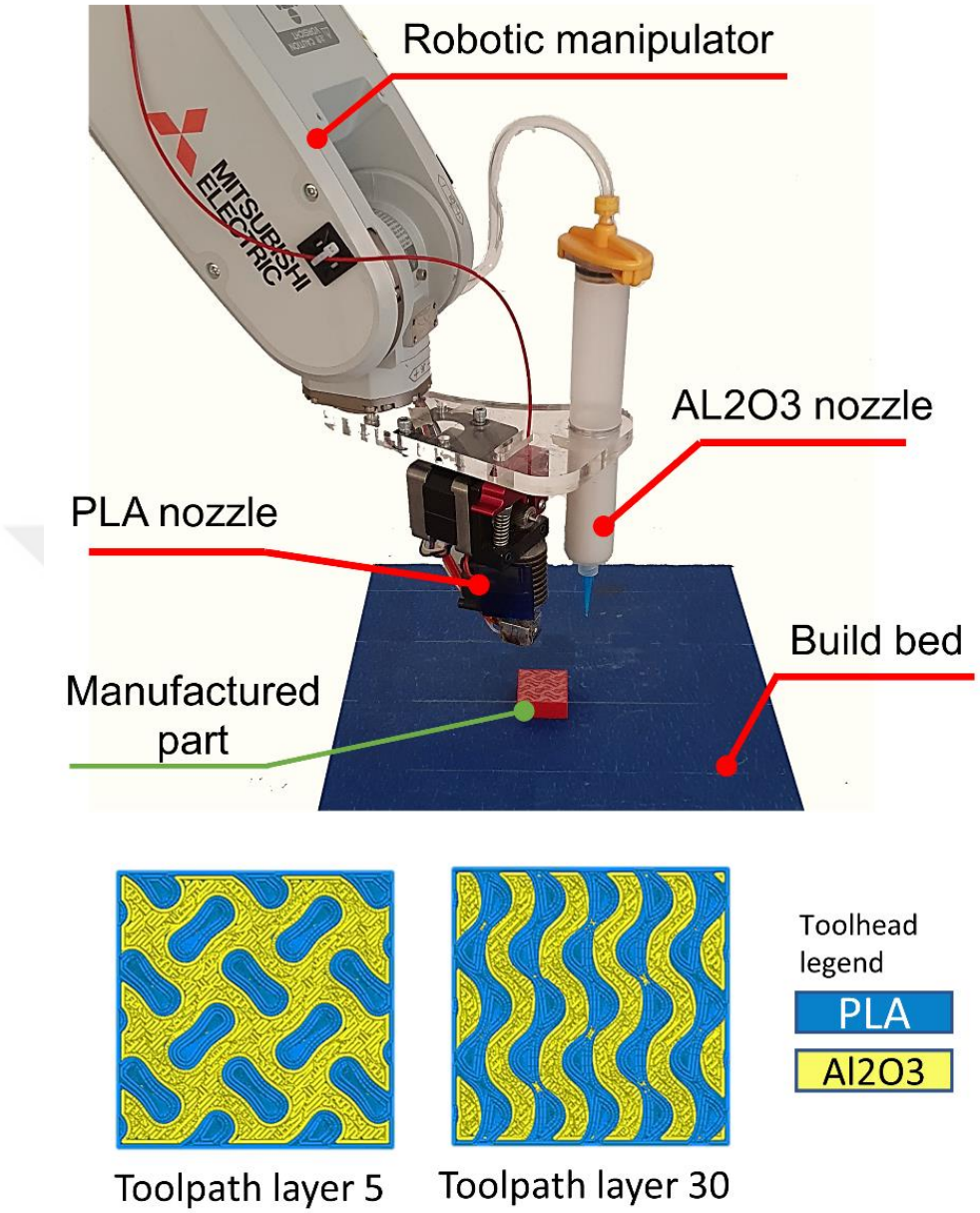

Figure 5.2. The multi-material additive manufacturing setup and the toolpaths for the multi-material additive manufacturing of Al_2O_3 ceramics.

5.2.5 Demolding

The ceramic green bodies are demolded from the additively manufactured mold by submerging in DCM. The DCM rapidly dissolves the PLA of the mold leaving behind the ceramic green body. The molded and demolded samples are illustrated in Figure 5.3.

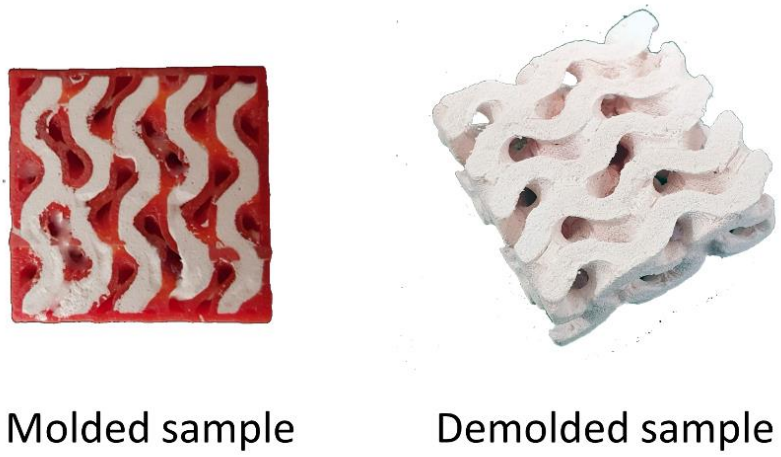

Figure 5.3. The molded sample was manufactured by multi-material additive manufacturing and the sample after demolding in dichloromethane.

5.2.6 Sintering regime

A multi-stage heating regime was adopted for the sintering of the ceramic green bodies inside a chamber furnace. The furnace was heated from room temperature to 300°C at the rate of 3°C/minute followed by an isothermal hold of 1 h for binder burnout. Next, the furnace was heated at 500°C at the rate of 3°C/minute followed by an isothermal 0.5 h to burn away any PLA that was left behind during the demolding process. In the final step, the furnace was heated to 1400°C at the rate of 5°C/minute followed by an isothermal hold of 3 h to sinter the green body. The sintered samples were retrieved from the furnace after the temperature of the furnace drops down to 30°C. The multi-stage sintering regime is illustrated in Figure 5.4.

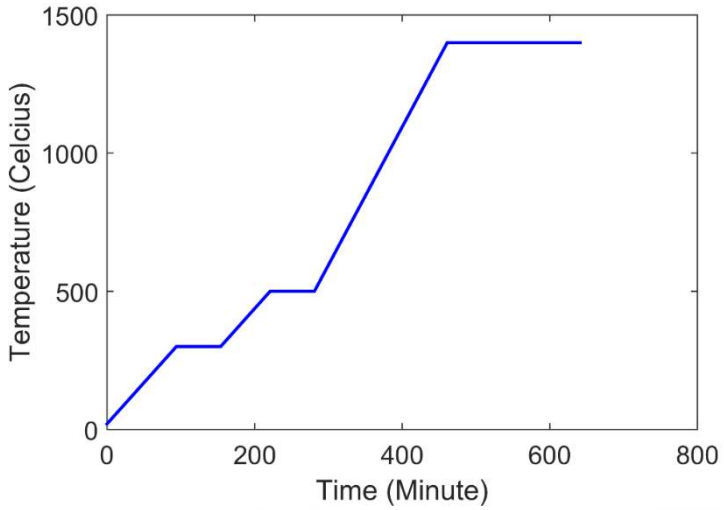

Figure 5.4. The multi-stage sintering regime.

5.3 Characterization

The rheology of the ceramic slurry was analyzed from 0.1 s^{-1} to 1000 s^{-1} at 20 ˚C on a Malvern Kineus pro rheometer. A parallel plate geometry of 25 mm diameter with a compatible solvent trap was used at a gap of 0.3 mm. The density of the sintered ceramic body was measured using the water retention technique. The morphologies of the sintered ceramics were studied using a ZEISS Ultra Plus Field Emission Scanning Electron Microscope (SEM). The X-ray diffractograms (XRD) were obtained using a Bruker D2 Phaser – X-ray Diffractometer with a Cu Kα1 radiation source using a wavelength of 1.54 Å. The power rating of the X-Ray generator was set to 30 kV at 10 mA current. Lynxeye detector with a slit size of 1 mm was used. The diffractograms were obtained within the 2θ range of 5˚ to 90˚ using a step size of 0.0204˚. The microhardness of the ceramic samples was characterized using Shimadzu HMV-G Series Micro Vickers hardness tester.

5.3.1 Rheology of ceramics slurry

The evolution of viscosity and shear stress as a function of shear rate was recorded at a logarithmic spacing of 10 data points per decade. The viscosity of the ceramic slurry is illustrated in Figure 5.5.

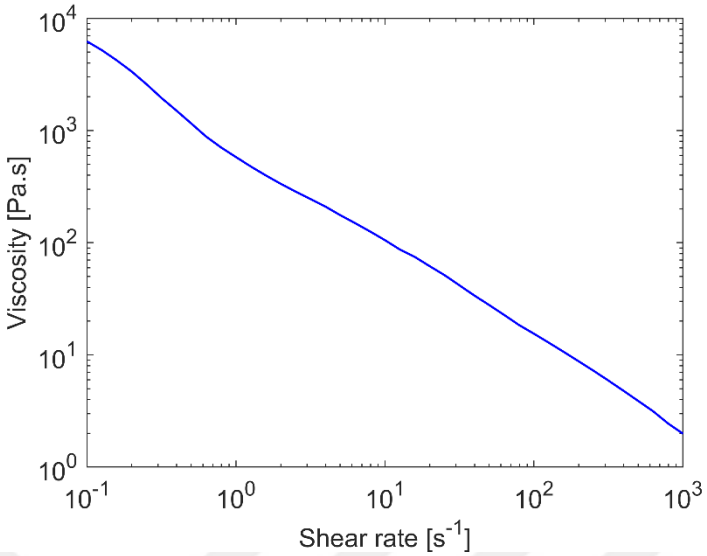

Figure 5.5. The viscosity of the ceramic slurry versus the shear rate.

The ceramic slurry demonstrates a non-Newtonian shear thinning behavior as the viscosity of the slurry decreases with the increase in the shear rate.

The shear stress versus shear rate curve of the slurry is illustrated in Figure 5.6.

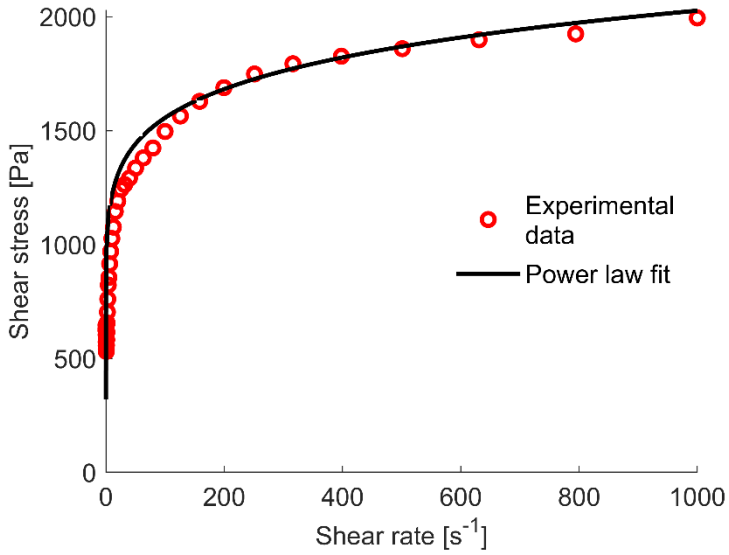

Figure 5.6. The shear stress versus the shear rate of the ceramic slurry along with power-law fitting for Herschel–Bulkley fluid model.

The shear stress of non-Newtonian fluids follows the Herschel–Bulkley fluid model. The model defines shear stress τ as

$$\tau = \tau_o + k\dot{\gamma}^n \quad \text{Eq. 5.1}$$

where τ_o is the yield shear stress, k is the consistency index, $\dot{\gamma}$ is the shear rate and n is the flow index. The shear stress versus shear rate curve was fitted to the Herschel–Bulkley fluid model to obtain the yield shear stress, the consistency, and the flow indices of the slurry. The shear stress of the slurry is modeled as

$$\tau = 320 + 649\,\dot{\gamma}^{0.14} \quad \text{Eq. 5.2}$$

5.3.2 Density

The true volume of the sintered body was measured using the Archimedes immersion technique and the pore volume was measured using the water retention technique. The apparent and true density of the sintered sample can be calculated by the following equations

$$V_{true} = \frac{m_{air} - m_{submerged}}{\rho_{fluid}} \quad \text{Eq. 5.3}$$

$$m_{retained\ fluid} = m_{saturated} - m_{oven\ dried} \quad \text{Eq. 5.4}$$

$$V_{pore} = \frac{m_{retained\ fluid}}{\rho_{fluid}} \quad \text{Eq. 5.5}$$

$$\rho_{ap} = \frac{m_{air}}{V_{true} + V_{pore}} \quad \text{Eq. 5.6}$$

$$\rho_{true} = \frac{m_{air}}{V_{true}} \quad \text{Eq. 5.7}$$

The apparent density ρ_{ap} of the sintered body was found to be 2.04 g/cm^3. The theoretical density of Al_2O_3 is 3.95 g/cm^3 therefore, the density of the sintered sample is about 51.64% of the theoretical value which corresponds to the porosity of 48.36%. however, the porosity of the sample was measured to be 48.25%. The slight deviation from the theoretical value can be attributed to impurities in the sample and the variance of the measurement technique.

5.3.3 Morphology

The SEM images reveal a well sintered porous structure of the samples. The SEM images at various magnifications are illustrated in Figure 5.7.

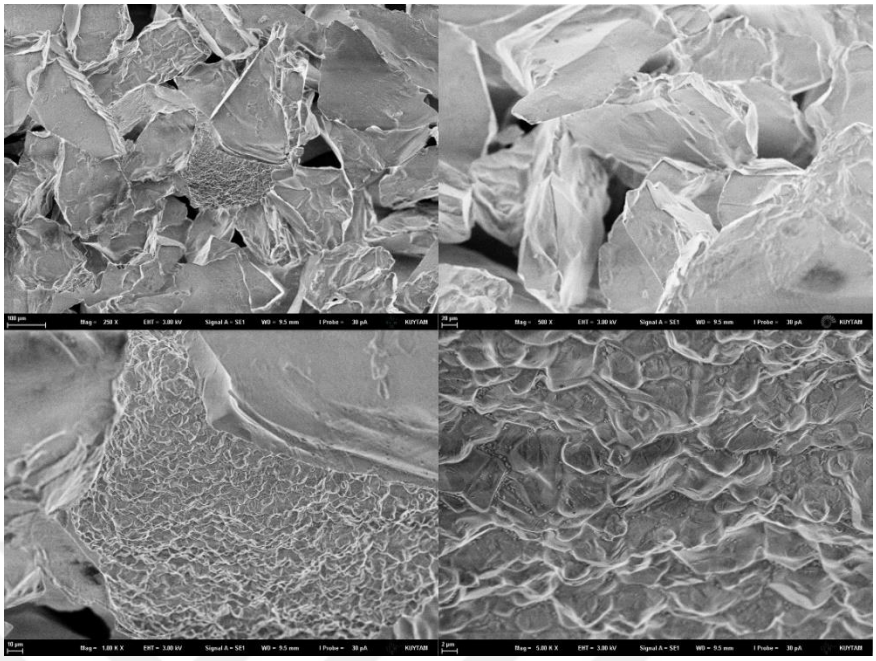

Figure 5.7. The morphology of the sintered ceramic body at various magnifications.

5.3.4 X-Ray Diffractogram

The X-ray diffractogram of the raw power and the sintered ceramic body is illustrated in Figure 5.8. The diffractogram of the Al_2O_3 powder indicates slight amorphousness which is expected in the powder; however, the amorphousness disappears in the sintered sample which indicates that the sample has completely sintered. The absence of any new peak indicates the absence of any chemical change during the sintering process.

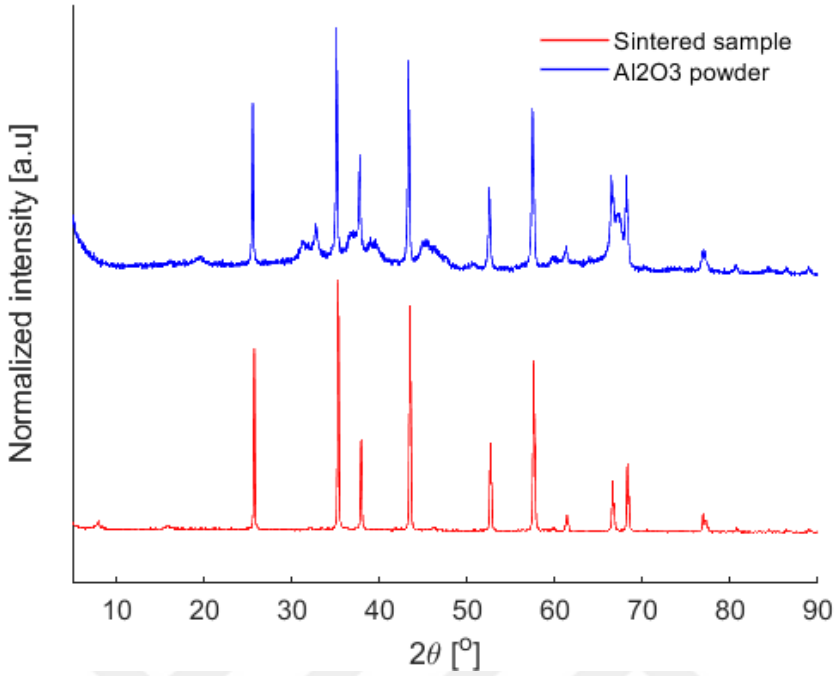

Figure 5.8. The X-ray diffractograms of the unsintered powder and the sintered ceramic body.

5.3.5 Microhardness testing

The microhardness hardness testing was carried out with a load of 490.3 mN with a hold time of 15 seconds using a 136° indenter. The microhardness of the sintered sample was found to be 1017 $\pm$ 20 HV.

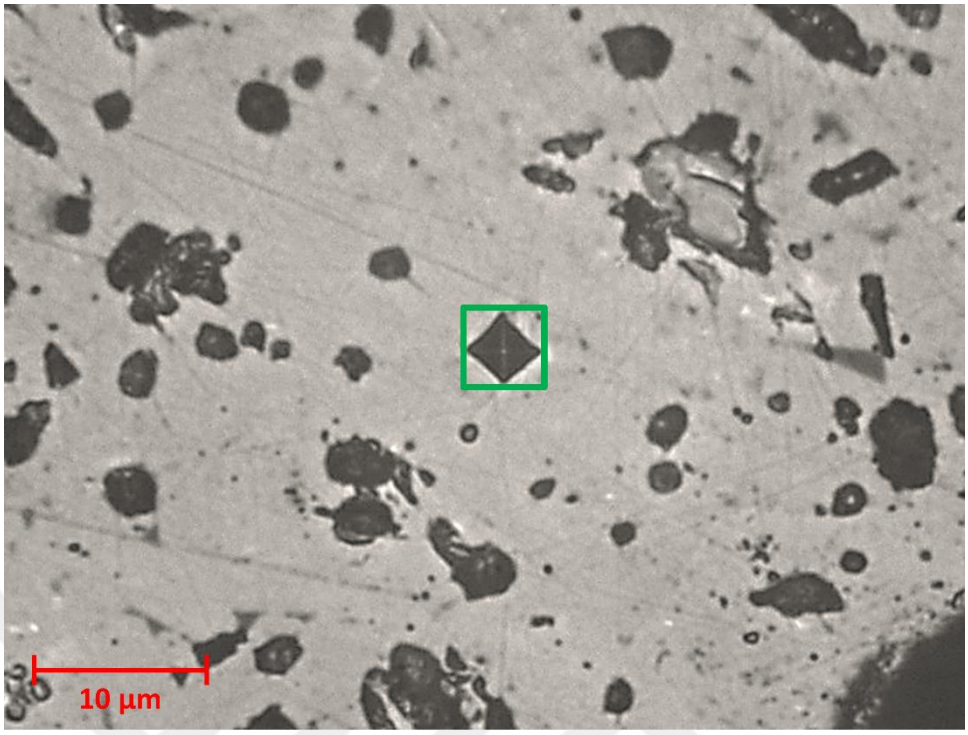

Figure 5.9. Indentation micrographs for the microhardness testing.

The hardness of Al_2O_3 highly depends on the processing conditions and the degree of densification. The harness of 98% dense Al_2O_3 is reported to be 1697 HV [70]. The lower hardness of the sintered sample can be attributed to its porosity. Nevertheless, the hardness of 1017 HV can be utilized in various applications such as dental implants as the harness of the enamel of human teeth is 274.8 HV [71]. The porosity of the sample plays a vital role in its hardness, therefore, the hardness of the sample can be modified by modifying the porosity of the samples.

5.4 Conclusion

The ability to manufacture ceramic bodies in complex geometries demonstrates the ability of the multi-material additive manufacturing technique. The technique demonstrated in this chapter utilizes aluminum oxide slurry however, the technique can be utilized to manufacture ceramic bodies from powders of various oxide type ceramics such as zirconium oxide and titanium oxide. The technique can be modified for non-oxide-type ceramics such as nitrides and borides by using furnaces with inner chambers to avoid oxidation during the sintering process.

Chapter 6

CONCLUSION

6.1 Overview

In summary, this thesis demonstrates the potential of additive manufacturing using functional materials. The MARC multi-material robotic additive manufacturing setup is capable of depositing various types of material in a single build.

An additively manufacturable and electrically conductive polymer composite (ePMC) was developed with tunable electrical conductivity based on the concentration of graphite loading. The developed ePMCs were characterized using various characterization techniques such as scanning electron microscopy (SEM), infrared spectroscopy (FTIR), X-ray diffraction (XRD), and two-point electrical conductivity.

The ePMC allows the additive manufacturing of application-specific heating elements and capacitive sensors. The moderate electrical conductivity of the ePMC allows for the development of capacitive sensors that can be dually used as a heater, and therefore, enables the development of hybrid systems.

An application of the developed ePMCs is presented for the development of an additively manufacturable smart disinfection system to contain the spread of SARS-CoV-2 in workspaces. The common use types of equipment in a workspace are interacted by multiple users and therefore, they can lead to the transmission of the virus. The smart disinfection system can detect user interaction with common-use equipment and thermally disinfect them.

Ceramics are used in various functional applications such as refractory, dielectric, and corrosion resistance. Additive manufacturing using ceramic material enables the realization of ceramic bodies in complex geometries which cannot be manufactured using conventional techniques.

A multi-material additive manufacturing approach is present that involves the layer-by-layer manufacturing of molds made from PLA. The ceramic slurry is cast into the molds gradually as the layers are built. The mold enhances the shape retention of the ceramic slurry. The additively manufactured ceramic green body is demolded by dissolving the mold in an organic solvent. The demolded green body is sintered at 1400°C in a chamber furnace to obtain the final ceramic body.

Ceramic bodies of high density and hardness were additively manufactured using the multi-material additive manufacturing technique. The additively manufactured ceramics were characterized using various characterization techniques such as SEM, XRD, Achemides density, and microhardness.

6.2 Recommendations for future work

The developed ePMC has the potential to be used for the manufacturing of customized antennas for the transmission and contraction of signals and the development of capacitive sensors for gesture recognition. These avenues could be investigated in future works.

The developed multi-material additive manufacturing approach has the potential for the additive manufacturing of various ceramics, metallic alloys, metal matrix composites, and ceramic matrix composites. These applications could be investigated in future works.

BIBLIOGRAPHY

1. ASTM F2792-12 (2012) Standard Terminology for Additive Manufacturing Technologies. ASTM Int.

2. Guo N, Leu MC (2013) Additive manufacturing: Technology, applications and research needs. Front Mech Eng 8:215–243. https://doi.org/10.1007/s11465-013-0248-8

3. Han P (2017) Additive Design and Manufacturing of Jet Engine Parts. Engineering 3:648–652. https://doi.org/10.1016/J.ENG.2017.05.017

4. Levesque JN, Shah A, Ekhtiari S, et al (2020) Three-dimensional printing in orthopaedic surgery: A scoping review. EFORT Open Rev. 5:430–441

5. Weller TR, Weller DR, Rodrigues LC de A, Volpato N (2021) A framework for tool-path airtime optimization in material extrusion additive manufacturing. Robot Comput Integr Manuf 67:101999. https://doi.org/10.1016/j.rcim.2020.101999

6. Shaqour B, Abuabiah M, Abdel-Fattah S, et al (2021) Gaining a better understanding of the extrusion process in fused filament fabrication 3D printing: a review. 114:1279–1291

7. Krishnanand, Taufik M (2021) Fused Filament Fabrication (FFF) Based 3D Printer and Its Design: A Review. In: Lecture Notes in Mechanical Engineering. Springer Science and Business Media Deutschland GmbH, pp 497–505

8. Ngo TD, Kashani A, Imbalzano G, et al (2018) Additive manufacturing (3D printing): A review of materials, methods, applications and challenges. Compos Part B Eng 143:172–196. https://doi.org/10.1016/J.COMPOSITESB.2018.02.012

9. Wang X, Jiang M, Zhou Z, et al (2017) 3D printing of polymer matrix composites: A review and prospective. Compos Part B Eng 110:442–458. https://doi.org/10.1016/J.COMPOSITESB.2016.11.034

10. Flowers PF, Reyes C, Ye S, et al (2017) 3D printing electronic components and circuits with conductive thermoplastic filament. Addit Manuf 18:156–163. https://doi.org/10.1016/J.ADDMA.2017.10.002

11. MacDonald E, Espalin D, Doyle D, et al (2018) Fabricating patch antennas within complex dielectric structures through multi-process 3D printing. J Manuf Process 34:197–203. https://doi.org/10.1016/J.JMAPRO.2018.05.013

12. Helena D, Ramos A, Varum T, Matos JN (2020) Antenna design using modern additive manufacturing technology: A review. IEEE Access 8:177064–177083. https://doi.org/10.1109/ACCESS.2020.3027383

13. Wei X, Li D, Jiang W, et al (2015) 3D Printable Graphene Composite. Sci Rep 5:11181. https://doi.org/10.1038/srep11181

14. Tan JC, Low HY (2018) Embedded electrical tracks in 3D printed objects by fused filament fabrication of highly conductive composites. Addit Manuf 23:294–302. https://doi.org/10.1016/J.ADDMA.2018.06.009

15. Singh R, Singh H, Farina I, et al (2019) On the additive manufacturing of an energy storage device from recycled material. Compos Part B Eng 156:259–265. https://doi.org/10.1016/J.COMPOSITESB.2018.08.080

16. Sezer HK, Eren O (2019) FDM 3D printing of MWCNT re-inforced ABS nano-composite parts with enhanced mechanical and electrical properties. J Manuf Process 37:339–347. https://doi.org/10.1016/J.JMAPRO.2018.12.004

17. Ambrosi A, Pumera M (2016) 3D-printing technologies for electrochemical applications. Chem Soc Rev 45:2740–2755. https://doi.org/10.1039/C5CS00714C

18. Farahani RD, Dalir H, Le Borgne V, et al (2012) Direct-write fabrication of freestanding nanocomposite strain sensors. Nanotechnology 23:085502. https://doi.org/10.1088/0957-4484/23/8/085502

19. Zhong J, Zhou G-X, He P-G, et al (2017) 3D printing strong and conductive geo-polymer nanocomposite structures modified by graphene oxide. Carbon N Y 117:421–426. https://doi.org/10.1016/J.CARBON.2017.02.102

20. Areir M, Xu Y, Zhang R, et al (2017) A study of 3D printed active carbon electrode for the manufacture of electric double-layer capacitors. J Manuf Process 25:351–356. https://doi.org/10.1016/J.JMAPRO.2016.12.020

21. ProtoPlant Electrically Conductive Composite PLA – ProtoPlant, makers of Proto-pasta. https://www.proto-pasta.com/products/conductive-pla?variant=1265211476. Accessed 18 Jun 2019

22. BLACKMAGIC3D Conductive Graphene 3D Printing PLA Filament. https://www.blackmagic3d.com/Conductive-p/grphn-pla.htm. Accessed 17 Jun 2019

23. Multi3D Electrifi Conductive Filament | Multi3D. https://www.multi3dllc.com/product/electrifi/. Accessed 18 Jun 2019

24. Pandey JK, Takagi H, Nakagaito AN, et al (2012) An overview on the cellulose based conducting composites. Compos Part B Eng 43:2822–2826. https://doi.org/10.1016/J.COMPOSITESB.2012.04.045

25. Li J, Lewis RB, Dahn JR (2007) Sodium Carboxymethyl Cellulose. Electrochem Solid-State Lett 10:A17. https://doi.org/10.1149/1.2398725

26. Benchabane A, Bekkour K (2008) Rheological properties of carboxymethyl cellulose (CMC) solutions. Colloid Polym Sci 286:1173–1180. https://doi.org/10.1007/s00396-008-1882-2

27. Padture NP (2016) Advanced structural ceramics in aerospace propulsion. Nat Mater 15:804

28. Zocca A, Colombo P, Gomes CM, Günster J (2015) Additive Manufacturing of Ceramics: Issues, Potentialities, and Opportunities. J Am Ceram Soc 98:1983–2001. https://doi.org/10.1111/jace.13700

29. Lakhdar Y, Tuck C, Binner J, et al (2021) Additive manufacturing of advanced

ceramic materials. Prog. Mater. Sci. 116

30. Chen Z, Li Z, Li J, et al (2019) 3D printing of ceramics: A review. J Eur Ceram Soc 39:661–687. https://doi.org/10.1016/j.jeurceramsoc.2018.11.013

31. Feilden E, Blanca EGTG-T, Giuliani F, et al (2016) Robocasting of structural ceramic parts with hydrogel inks. J Eur Ceram Soc 36:2525–2533. https://doi.org/10.1016/j.jeurceramsoc.2016.03.001

32. Rueschhoff L, Costakis W, Michie M, et al (2016) Additive Manufacturing of Dense Ceramic Parts via Direct Ink Writing of Aqueous Alumina Suspensions. Int J Appl Ceram Technol 13:821–830. https://doi.org/10.1111/ijac.12557

33. M'Barki A, Bocquet L, Stevenson A, et al (2017) Linking Rheology and Printability for Dense and Strong Ceramics by Direct Ink Writing. Sci Rep 7:1–10. https://doi.org/10.1038/s41598-017-06115-0

34. Yu T, Zhang Z, Liu Q, et al (2019) Extrusion-based additive manufacturing of yttria-partially-stabilized zirconia ceramics. https://doi.org/10.1016/j.ceramint.2019.10.245

35. Lopez CD, Diaz-Siso JR, Witek L, et al (2018) Three dimensionally printed bioactive ceramic scaffold osseoconduction across critical-sized mandibular defects. J Surg Res 223:115–122

36. Nan B, Gołębiewski P, Buczyński R, et al (2020) Direct Ink Writing Glass: A Preliminary Step for Optical Application. Materials (Basel) 13:1636

37. Lu R, Chandrasekaran S, Du Frane WL, et al (2018) Complex shaped boron carbides from negative additive manufacturing. Mater Des 148:8–16. https://doi.org/10.1016/j.matdes.2018.03.026

38. Li W, Armani A, McMillen D, et al (2020) Additive manufacturing of zirconia parts with organic sacrificial supports. Int J Appl Ceram Technol

39. Lin R, Li A, Lu L, Cao Y (2015) Preparation of bulk sodium carboxymethyl cellulose aerogels with tunable morphology. Carbohydr Polym 118:126–132. https://doi.org/10.1016/J.CARBPOL.2014.10.075

40. Khaled B, Abdelbaki B (2012) Rheological and electrokinetic properties of carboxymethylcellulose-water dispersions in the presence of salts. Int J Phys Sci 7:1790–1798. https://doi.org/10.5897/IJPS11.1779

41. Kaur G, Adhikari R, Cass P, et al (2015) Electrically conductive polymers and composites for biomedical applications. RSC Adv 5:37553–37567. https://doi.org/10.1039/C5RA01851J

42. Marinho B, Ghislandi M, Tkalya E, et al (2012) Electrical conductivity of compacts of graphene, multi-wall carbon nanotubes, carbon black, and graphite powder. Powder Technol 221:351–358. https://doi.org/10.1016/J.POWTEC.2012.01.024

43. Foo CY, Lim HN, Mahdi MA, et al (2018) Three-Dimensional Printed Electrode and Its Novel Applications in Electronic Devices. Sci Rep 8:. https://doi.org/10.1038/s41598-018-25861-3

44. Isa MA, Lazoglu I (2019) Five-axis additive manufacturing of freeform models through buildup of transition layers. J Manuf Syst 50:69–80. https://doi.org/10.1016/J.JMSY.2018.12.002

45. Yigit IE, Lazoglu I (2019) Helical slicing method for material extrusion-based robotic additive manufacturing. Prog Addit Manuf 4:225–232. https://doi.org/10.1007/s40964-019-00090-w

46. Malik AN, Khan SA, Lazoglu I (2020) A novel hybrid frost detection and defrosting system for domestic refrigerators. Int J Refrig. https://doi.org/10.1016/j.ijrefrig.2020.05.016

47. Kampf G, Todt D, Pfaender S, Steinmann E (2020) Persistence of coronaviruses on inanimate surfaces and their inactivation with biocidal agents. J. Hosp. Infect. 104:246–251

48. Slifka MK, Gao L (2020) Is presymptomatic spread a major contributor to COVID-19 transmission? Nat. Med. 26:1531–1533

49. Wilson AM, Verhougstraete MP, Beamer PI, et al (2021) Frequency of hand-to-head, -mouth, -eyes, and -nose contacts for adults and children during eating and

non-eating macro-activities. J Expo Sci Environ Epidemiol 31:34–44. https://doi.org/10.1038/s41370-020-0249-8

50. Chen B, Han J, Dai H, Jia P (2021) Biocide-tolerance and antibiotic-resistance in community environments and risk of direct transfers to humans: Unintended consequences of community-wide surface disinfecting during COVID-19? Environ Pollut 283:117074. https://doi.org/10.1016/j.envpol.2021.117074

51. Murthy GS (2020) An Automatic Disinfection System for Passenger Luggage at Airports and Train/Bus Stations. Trans Indian Natl Acad Eng 5:295–298. https://doi.org/10.1007/s41403-020-00131-9

52. Mahida N, Vaughan N, Boswell T (2013) First UK evaluation of an automated ultraviolet-C room decontamination device (Tru-D^{TM}). J Hosp Infect 84:332–335. https://doi.org/10.1016/j.jhin.2013.05.005

53. Yang JH, Wu UI, Tai HM, Sheng WH (2019) Effectiveness of an ultraviolet-C disinfection system for reduction of healthcare-associated pathogens. J Microbiol Immunol Infect 52:487–493. https://doi.org/10.1016/j.jmii.2017.08.017

54. Borschel GH, Daeschler SC, Manson N, et al (2020) Reprocessing N95 respirators during the COVID-19 pandemic: Moist heat inactivates SARS-CoV-2 and maintains N95 filtration. medRxiv 2020.05.25.20112615

55. Yu L, Peel GK, Cheema FH, et al (2020) Catching and killing of airborne SARS-CoV-2 to control spread of COVID-19 by a heated air disinfection system. Mater Today Phys 15:100249. https://doi.org/10.1016/j.mtphys.2020.100249

56. The heat is on: High temps tested for killing viruses in the flight deck. https://www.boeing.com/confident-travel/story.html?id=thermal-disinfection. Accessed 17 Feb 2021

57. Abraham JP, Plourde BD, Cheng L (2020) Using heat to kill SARS-CoV-2. Rev Med Virol 30:8–10. https://doi.org/10.1002/rmv.2115

58. Kampf G, Voss A, Scheithauer S (2020) Inactivation of coronaviruses by heat. J. Hosp. Infect. 105:348–349

59. Hagqvist P, Heralić A, Christiansson AK, Lennartson B (2015) Resistance based iterative learning control of additive manufacturing with wire. Mechatronics 31:116–123. https://doi.org/10.1016/j.mechatronics.2015.03.008

60. Khan SA, Lazoglu I (2020) Development of additively manufacturable and electrically conductive graphite–polymer composites. Prog Addit Manuf 5:153–162. https://doi.org/10.1007/s40964-019-00102-9

61. BS EN 13202:2000 (2000) Ergonomics of the thermal environment - Temperatures of touchable hot surfaces - Guidance for establishing surface temperature limit values in production standards with the aid of EN 563

62. Seminara L, Pinna L, Ibrahim A, et al (2016) Towards integrating intelligence in electronic skin. Mechatronics 34:84–94. https://doi.org/10.1016/j.mechatronics.2015.04.001

63. Luo S, Bimbo J, Dahiya R, Liu H (2017) Robotic tactile perception of object properties: A review. Mechatronics 48:54–67

64. Gentile C, Cordella F, Rodrigues CR, Zollo L (2020) Touch-and-slippage detection algorithm for prosthetic hands. Mechatronics 70:102402. https://doi.org/10.1016/j.mechatronics.2020.102402

65. Rochus V, Wang B, Tilmans HAC, et al (2016) Fast analytical design of MEMS capacitive pressure sensors with sealed cavities. Mechatronics 40:244–250. https://doi.org/10.1016/j.mechatronics.2016.05.012

66. Wang CY, Cai DC (2017) Hand tool handle design based on hand measurements. In: MATEC Web of Conferences

67. Sunaga T, Ikehira H, Furukawa S, et al (2002) Measurement of the electrical properties of human skin and the variation among subjects with certain skin conditions. Phys Med Biol 47:11–15. https://doi.org/10.1088/0031-9155/47/1/402

68. Salahuddin S, Porter E, Krewer F, O' Halloran M (2017) Optimised analytical models of the dielectric properties of biological tissue. Med Eng Phys 43:103–111. https://doi.org/10.1016/j.medengphy.2017.01.017

69. Gray T (2019) Self Capacitance. In: Projected Capacitive Touch. Springer International Publishing, pp 19–25

70. Žmak I, Ćorić D, Mandić V, Ćurković L (2020) Hardness and indentation fracture toughness of slip cast alumina and alumina-zirconia ceramics. Materials (Basel) 13:122. https://doi.org/10.3390/ma13010122

71. Chun KJ, Choi HH, Lee JY (2014) Comparison of mechanical property and role between enamel and dentin in the human teeth. J Dent Biomech 5:1–7. https://doi.org/10.1177/1758736014520809